

High-definition spatial transcriptomic profiling of immune cell populations in colorectal cancer

Received: 13 June 2024

Accepted: 14 April 2025

Published online: 5 June 2025

 Check for updates

Michelli Faria de Oliveira^{1,2}, Juan Pablo Romero ^{1,2}, Meii Chung^{1,2}, Stephen R. Williams¹, Andrew D. Gottscho ¹, Anushka Gupta ¹, Susan E. Pilipauskas¹, Seayar Mohabbat¹, Nandhini Raman ¹, David J. Sukovich¹, David M. Patterson¹, Visium HD Development Team* & Sarah E. B. Taylor ¹ 

A comprehensive understanding of cellular behavior and response to the tumor microenvironment (TME) in colorectal cancer (CRC) remains elusive. Here, we introduce the high-definition Visium spatial transcriptomic technology (Visium HD) and investigate formalin-fixed paraffin-embedded human CRC samples ($n = 5$). We demonstrate the high sensitivity, single-cell-scale resolution and spatial accuracy of Visium HD, generating a highly refined whole-transcriptome spatial profile of CRC samples. We identify transcriptomically distinct macrophage subpopulations in different spatial niches with potential pro-tumor and anti-tumor functions via interactions with tumor and T cells. In situ gene expression analysis validates our findings and localizes a clonally expanded T cell population close to macrophages with anti-tumor features. Our study demonstrates the power of high-resolution spatial technologies to understand cellular interactions in the TME and paves the way for larger studies that will unravel mechanisms and biomarkers of CRC biology, improving diagnosis and disease management strategies.

CRC accounted for 9.4% of cancer-related deaths (0.9 million) in 2020, and its global incidence is predicted to double by 2035 (refs. 1,2). Its poor 5-year survival rate highlights the need for better early detection and prognostic biomarkers for future disease management³. Growing evidence suggests that tumor heterogeneity is best described at the transcriptome level, rather than with classical histopathological or mutation-centered disease classifications⁴. Technologies that refine our understanding of the TME, including the diverse roles of innate and adaptive immune responses and cellular crosstalk in CRC, have the potential to inform better clinical intervention strategies.

Sequencing-based genomic technologies have played an important role in building our knowledge of CRC biology^{4–7}. However, bulk

sequencing, which involves averages data from cells and tissues, is confounded by the complexities of the TME and intratumor heterogeneity. Single-cell transcriptomic (single-cell RNA-sequencing (scRNA-seq)) technologies have partially filled this gap and allowed for detailed exploration of the cell types within the TME in CRC^{8–16}. Although these studies add critical single-cell-level resolution to our understanding of CRC, they lack any information about the cellular organization within the tissue. Spatial transcriptomics offers a solution. Several commercial technologies are currently available, including Visium CytAssist Spatial Gene Expression ('Visium v2', 10x Genomics), STOmics (BGI) and Curio Seeker (Curio Bioscience). Other published methods include Seq-Scope¹⁷, Nova-ST¹⁸, Open-ST¹⁹, HDST²⁰, DBiT-seq²¹, Pixel-seq²² and XYSeq²³. These methods have enabled the localization of cell types

¹10x Genomics, Inc, Pleasanton, CA, USA. ²These authors contributed equally: Michelli Faria de Oliveira, Juan Pablo Romero, Meii Chung. *A list of authors and their affiliations appears at the end of the paper.  e-mail: sarah.taylor@10xgenomics.com

within tissues, which is critical for understanding the interaction between cells in the TME of CRC^{24–27}. However, these technologies lack resolution at the single-cell scale or are typically only compatible with freshly frozen tissues, and, as such, a deep understanding of tumor organization based on readily available biobanked samples remains elusive.

Here, we introduce Visium HD Spatial Gene Expression (‘Visium HD’), a whole-transcriptome assay with single-cell-scale resolution compatible with freshly frozen, fixed frozen and formalin-fixed paraffin-embedded (FFPE) samples. The Visium HD slides provide a dramatically increased oligonucleotide barcode density (~11,000,000 continuous 2- μ m features in a 6.5 \times 6.5-mm Visium HD capture area, compared to ~5,000 55- μ m features with gaps between the equivalent Visium v2 capture area), generating data that can be binned in square features. We demonstrate the use of Visium HD as a discovery platform by profiling CRC FFPE tissue blocks from multiple patients. The single-cell-scale resolution of Visium HD allowed us to map distinct populations of immune cells, specifically macrophages and T cells, and evaluate DGE at the tumor boundary. We also generated a multi-patient single-cell reference dataset from a larger cohort of FFPE samples and used it to annotate deconvolved Visium HD data bins, validating the cell type populations identified by Visium HD and subsequently using the integrated data to comprehensively map the cellular composition and molecular signatures of the TME in CRC. Leveraging the high resolution of Visium HD, we examined the cells at the immediate periphery (within 50 μ m) of the tumor. This allowed us to spatially map distinct macrophage subpopulations to specific tumor regions, to compare their transcriptomic profiles, which indicate that they may exert pro-tumor roles via different pathways, and to characterize cell–cell interactions. To validate the spatial accuracy of Visium HD, we analyzed a subset of genes using an independent spatial technology (Xenium In Situ Gene Expression²⁸). We confirmed the presence of the two pro-tumor macrophage subpopulations in different tumor niches and pinpointed the location of the T cells within the TME. We also detected a clonally expanded T cell population and the microenvironment in which it resides, revealing a macrophage-containing niche with anti-tumor features.

Our study underscores the importance of using high-resolution spatial technologies in exploring the heterogeneity of cancer biology. These advanced tools are crucial for precisely mapping diverse immune cell niches and elucidating the complex interactions between these cells and their microenvironment. Spatial technologies provide a detailed understanding of spatial variations in cell types, their subpopulations and cell-to-cell relationships, which are key to developing targeted therapies and personalized treatment approaches. The combination of whole-transcriptome and targeted in situ spatial technologies used in our investigation provides a deep insight into the complex and dynamic nature of the TME, highlighting the importance of spatial context in understanding cancer heterogeneity and disease progression.

Results

Visium HD enables transcriptome-wide spatial gene expression analysis at single-cell scale. Gene expression is measured by the capture of ligated probe pairs targeting the whole protein-coding transcriptome. We profiled tumor biopsies from five patients with colorectal adenocarcinoma, in addition to normal adjacent tissue (NAT) from three of these patients (Table 1). Serial sections of FFPE tissues were used to benchmark the technology performance or to explore the TME using Visium HD. Additionally, selected serial sections were used to generate an scRNA-seq dataset and for in situ gene expression analysis (Fig. 1).

Visium HD specifications and performance

The Visium HD capture array consists of 2 \times 2- μ m squares of uniquely barcoded oligonucleotides directly adjacent to each other on the slide,

resulting in a continuous lawn of capture oligonucleotides. This represents an increase of several orders of magnitude in barcode complexity over earlier Visium slides, which have 55- μ m circular capture areas with a 100- μ m center to center gaps between them (Fig. 2a,b). For downstream analysis, the Space Ranger (version 3.0) pipeline outputs the raw 2- μ m data and data binned at 8- and 16- μ m resolution. Unless otherwise described, we used the 8- μ m binned data in our analyses.

To assess Visium HD performance, we analyzed serial sections from a normal colon mucosa sample run on Visium v2 and Visium HD. Visium HD generated notably higher-resolution data, as shown by the improved unsupervised clustering, both in terms of the refined specificity of the clusters and the ability to map them to morphological features of the colon mucosal tissue (Fig. 2c). Whole-transcriptome unique molecular identifier (UMI) counts at similar sequencing depth showed a strong correlation between the two technologies (Fig. 2d, $R^2 = 0.82$ and Extended Data Fig. 1, $R^2 = 0.81$ and 0.90), indicating that the Visium HD assay maintains the high assay sensitivity of Visium v2 (Supplementary Table 1).

The estimated fraction of molecules arising from off-target probe binding events, that is, probes binding to genomic DNA (gDNA), was reduced in Visium HD (average of 4.13% in Visium v2 and 0.70% in Visium HD) (Supplementary Table 1). To assess any potential bias arising from such events, these probes were computationally excluded for this analysis, after which we observed a stronger correlation between the UMI counts from the different assays ($R^2 = 0.92$, Fig. 2d; $R^2 = 0.93$ and 0.96, Extended Data Fig. 1).

In array-based spatial technologies, the analyte to be measured (messenger RNA (mRNA) itself or a ligated probe reporting on the mRNA) must move from the tissue to come in contact with the array. Precise transfer of analytes with minimal lateral movement is essential to ensure that the spatial transcript measurements are representative of the biology of the tissue being analyzed. To achieve this, tissue placement and subsequent molecular biology reactions must be carefully controlled to minimize lateral movement of transcripts or their proxies away from the site of origin. Similar to the Visium v2 assay, Visium HD uses the CytAssist instrument. The CytAssist controls reagent flow and thus allows target molecules from the tissue to be captured upon release, preventing free diffusion of transcripts and ensuring accurate transfer of analytes from tissues to the capture arrays. The spatial fidelity gains afforded by the CytAssist have been described previously^{29,30} (technical note CG000618, revision B). To quantify the spatial accuracy of Visium HD, we analyzed genes with distinct localization to the glands of normal colon mucosal tissue (goblet cell gene markers: *CLCA1*, *FCGBP* and *MUC2*). In each tissue section, we manually selected four regions of interest (ROIs) and, for each marker gene, quantified the number of UMIs that were within or outside of the annotated structures in which their expression is expected based on established expression patterns³¹. We observed that most transcripts (98.3–99%) were localized in their expected morphological locations within the source masks, and only a small proportion (0.97–1.73%) were in adjacent masks (Fig. 2e and Extended Data Fig. 2), consistent with faithful transfer of ligated probes from the tissue to the array at single-cell-scale resolution.

Visium HD maps the landscape of CRC at single-cell scale

We profiled three CRC samples using Visium HD and combined them into a single dataset. An initial analysis of the combined dataset identified 23 clusters grouped into nine major cell types (tumor, intestinal epithelial, endothelial, smooth muscle, T cells, fibroblasts, B cells, myeloid, neuronal) and one unknown cluster (a cell cluster with a gene expression profile that did not readily match any known cell type), which aligned with the expected morphological features of the tissues (Fig. 3a). As an orthogonal measurement of cells present in normal and diseased colon samples, we generated a single-cell reference atlas of 260,506 cells from serial FFPE sections of normal and CRC tissues ($n = 8$; Table 1).

Table 1 | Samples evaluated in this study

Sample	Colon region	Stage	Sex	Age	Visium HD	Visium v2	Xenium	Chromium Flex	Chromium TCR
P1CRC	Rectum	II-A	F	72	Included		Included	Included	
P2CRC	Sigmoid	III-B	M	60	Included	Included	Included	Included	
P2NAT									
P3CRC	Transversum	III-B	M	83					Included
P3NAT					Included	Included			Included
P4CRC	Not specified	II-A	F	61					Included
P5CRC	Not specified	IV-A	F	58	Included		Included	Included	Included
P5NAT						Included			Included

NAT was available for P2, P3 and P5.

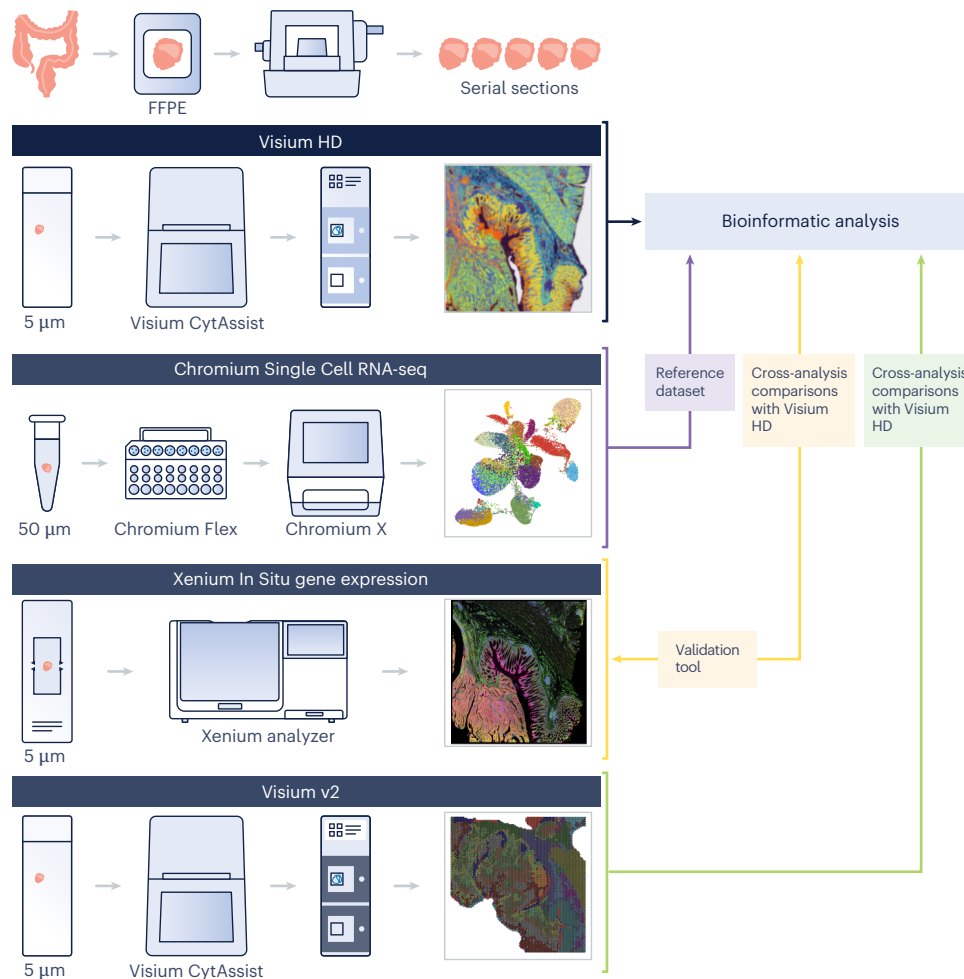


Fig. 1 | Analysis of CRC and NAT samples using Visium HD. Serial tissue sections were taken from colorectal adenocarcinoma (CRC, $n = 5$ samples) and NAT ($n = 3$ samples) FFPE blocks. A subset of samples were selected and analyzed with the Visium HD assay ($n = 3$ CRC and $n = 2$ NAT samples). Sections from the same FFPE blocks were assayed with scRNA-seq (Chromium Single Cell Gene Expression Flex; $n = 8$). Serial sections were analyzed with Xenium

In Situ Gene Expression ($n = 4$ CRC samples) and assayed via the Visium v2 assay ($n = 1$ CRC and $n = 2$ NAT samples). Single-cell data were used to create a reference dataset for cell type annotation. In situ data were used for validation of the findings from the Visium HD data and for subsequent analyses. Technology performance comparisons were made using data from matched datasets.

Differential gene expression (DGE) analysis of the cells in this atlas allowed us to annotate cell types based on published cell gene markers (Extended Data Fig. 3). We used this dataset as a reference to deconvolve the HD data, which yielded a highly resolved map of the cell types within the tissue resembling the expected tissue morphology (Fig. 3b). Each patient sample was associated with a major and distinct tumor cell type (Extended Data Figs. 4 and 5) that mapped onto the tumor regions across each tissue section. We validated the spatial arrangement of

these cell labels in Visium HD with the expression of well-known markers such as *PIGR* (goblet cells and enterocytes), *CEACAM6* (tumor) and *COL1A1* (fibroblasts) (Fig. 3c). When we compared the unsupervised clustering to the deconvolution results, we found that cell types with stereotypical morphological organization (for example, goblet cells and enterocytes in colon glands) can be identified based on the Visium HD clustering data alone. However, deconvolution based on single-cell data was useful for identifying subtypes of cells with a more random

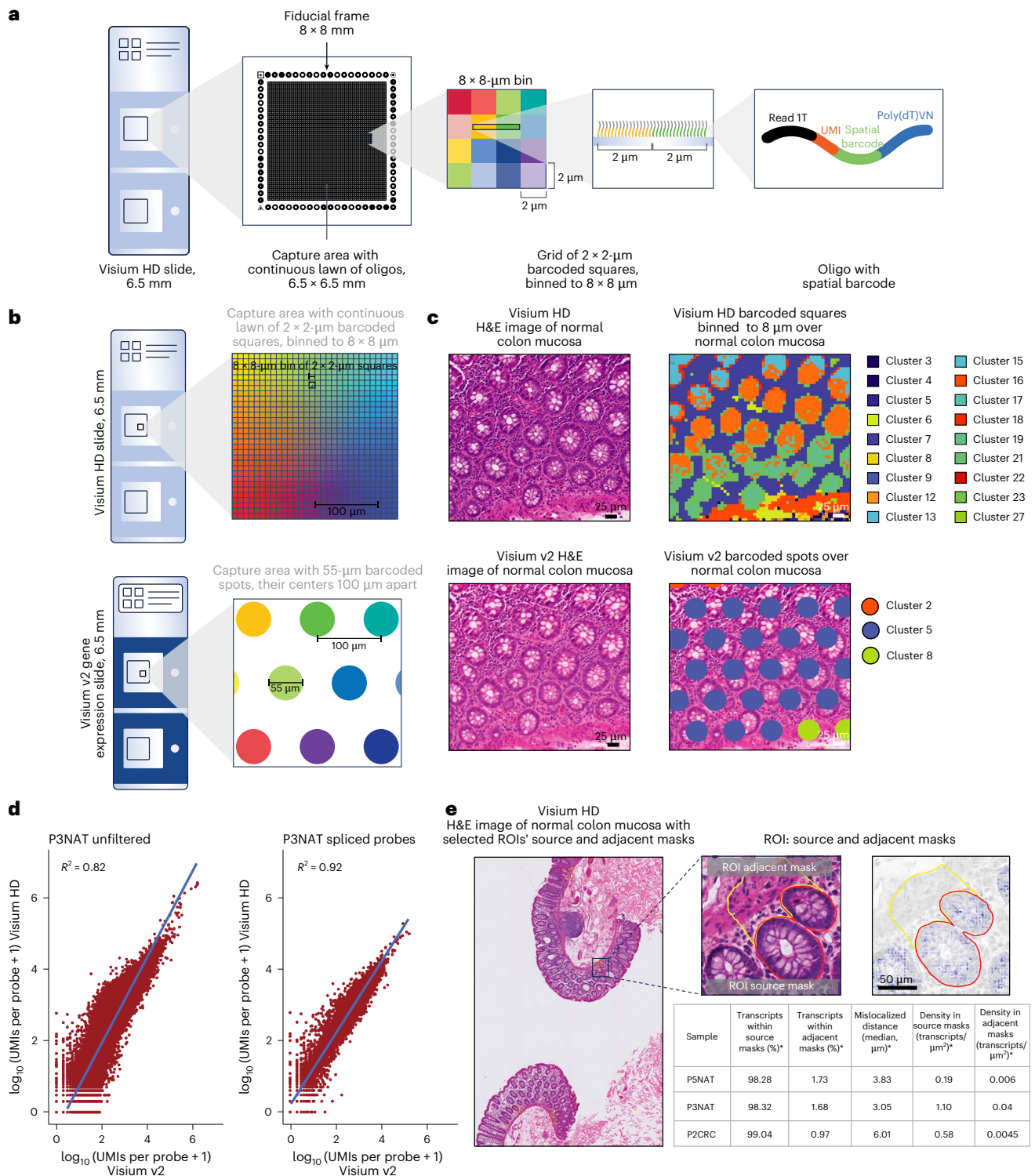


Fig. 2 | Visium HD Spatial Gene Expression slide architecture and performance.

a, Visium HD slide with two 6.5 × 6.5-mm capture areas, each containing a continuous lawn of uniquely barcoded 2 × 2-μm squares, which are binned to 8-μm squares for downstream analysis. Oligo, oligonucleotide; Read 1T, TruSeq Read 1; Poly(dT)VN, a string of T nucleotides followed by a variable nucleotide V (A, C or G) and then another variable nucleotide N (A, C, G or T). **b**, Visium HD slides, compared with Visium v2 slides, which have spots of 55 μm in diameter spaced 100 μm apart. **c**, Comparison of serial sections of a representative normal colon mucosa sample, P3NAT (one replicate). Visium HD detects 18 clusters that closely correspond to tissue morphology, while Visium v2 detects three clusters. H&E, hematoxylin and eosin. **d**, Sensitivity comparison between Visium HD and Visium v2 on the representative sample P3NAT. The left plot shows expression levels of

all probes (whole transcriptome); the right plot shows only probes spanning an exon–exon splice junction. Diagonal lines represent $x = y$. **e**, Transcript localization accuracy analysis performed across four randomly selected ROIs per tissue section (three independent samples, one replicate per sample) for selected goblet cell gene markers (*CLCA1*, *FCGBP* and *MUC2*); source masks are colon gland structures, and adjacent masks are the immediately adjacent regions containing lamina propria. Images show selected ROIs in a representative normal sample, P3NAT (one replicate); red lines outline the source mask, and yellow lines outline the adjacent mask. Table shows the median percentage of localized transcripts in the source and adjacent masks, the density of selected transcripts in both masks and the distance of selected transcripts from source masks (*). Four ROIs in each colon sample were included in this analysis.

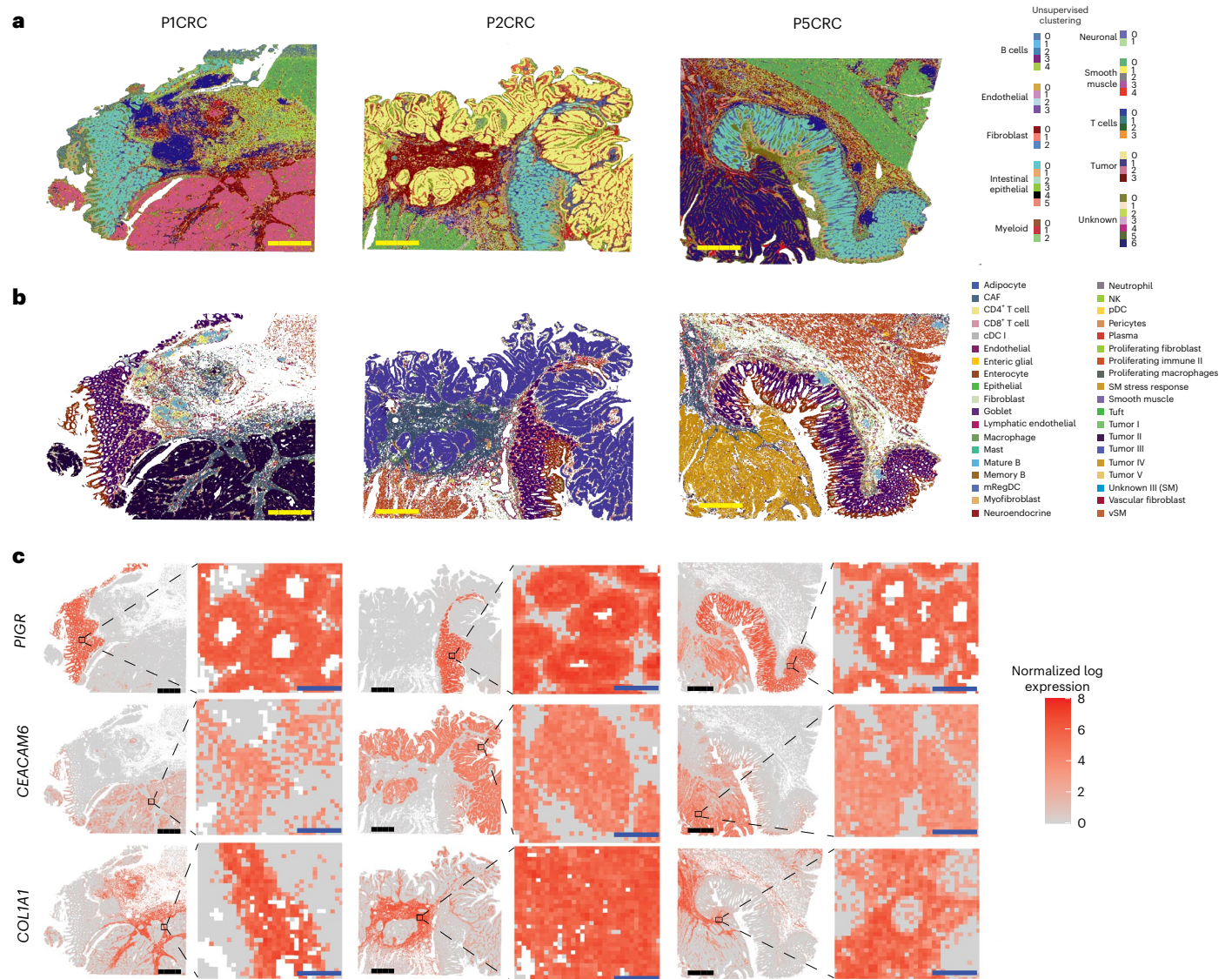


Fig. 3 | Spatial mapping of CRC samples using Visium HD reveals high-resolution, accurate transcript mapping. **a**, Spatial mapping of three CRC samples (P1CRC, P2CRC and P5CRC) with 8- μ m bins colored based on unsupervised clustering labels (level 2 labels) via sketch analysis. **b**, Spatial mapping of the same three CRC samples with 8- μ m bins colored by cell types predicted by deconvolution using the single-cell reference dataset. cDC, conventional dendritic cell; mRegDC, mature dendritic cell

enriched in immunoregulatory molecules; NK, natural killer cell; pDC, plasmacytoid dendritic cell; SM, smooth muscle; vSM, vascular smooth muscle. **c**, Corroboration of selected cellular gene markers with known spatial localization: *PIGR* (goblet cells and enterocytes), *CEACAM6* (tumor) and *COL1A1* (fibroblasts). Samples correspond to those in **a**. For each sample, the tissue-level view is shown on the left, with the inset as a black box, and the inset view is shown on the right. Scale bars, 1 mm (yellow or black), 80 μ m (blue).

organization or very small cells, for example, B cell and T cell subtypes (Extended Data Fig. 6).

Tumor boundary analysis reveals macrophage subpopulations
As immune cell dynamics are known to play a key role in CRC progression, we used the Visium HD data to characterize the immune cell populations proximal to tumor cells. We used a custom distance-based analysis to identify all barcoded 8- μ m bins within 50 μ m of the regions we had labeled as tumor cells via spot deconvolution (Fig. 4a). We reasoned that a 50- μ m radius around tumor cells was likely to contain cells that are either directly interacting with the tumor cells or influencing the TME. We quantified the cellular composition of these regions compared to those identified in the rest of the tissue. In all tissue blocks, cancer-associated fibroblasts (CAFs) were the most prominent cell type while macrophages were consistently identified as the most abundant immune cell type (Fig. 4b) in regions proximal to tumor cells. We

corroborated these findings by examining the expression of known macrophage (*CIQC*) and CAF (*COL1A1*) markers (Fig. 4a).

As the most abundant immune cell type in the tumor periphery, we focused our analysis on the macrophage populations. We identified two macrophage subpopulations with specific gene expression profiles mainly defined by expression of *SELENOP* or *SPPI* genes (Fig. 4c). Density estimation analysis revealed that the highly enriched regions of these macrophage subpopulations in the TME were mostly in distinct spatial niches (Fig. 4d). To gain insights on the potential role of these spatially specific macrophages in the TME, we performed an enrichment analysis of the differentially expressed genes. We observed that *SELENOP*⁺ macrophages were enriched for pathways involved in processes such as inflammatory response, tumor necrosis factor (TNF) signaling via NF- κ B, apoptosis, and response to ultraviolet radiation. Meanwhile, *SPPI*⁺ macrophages were enriched for genes involved in coagulation, cholesterol homeostasis and upregulation of KRAS

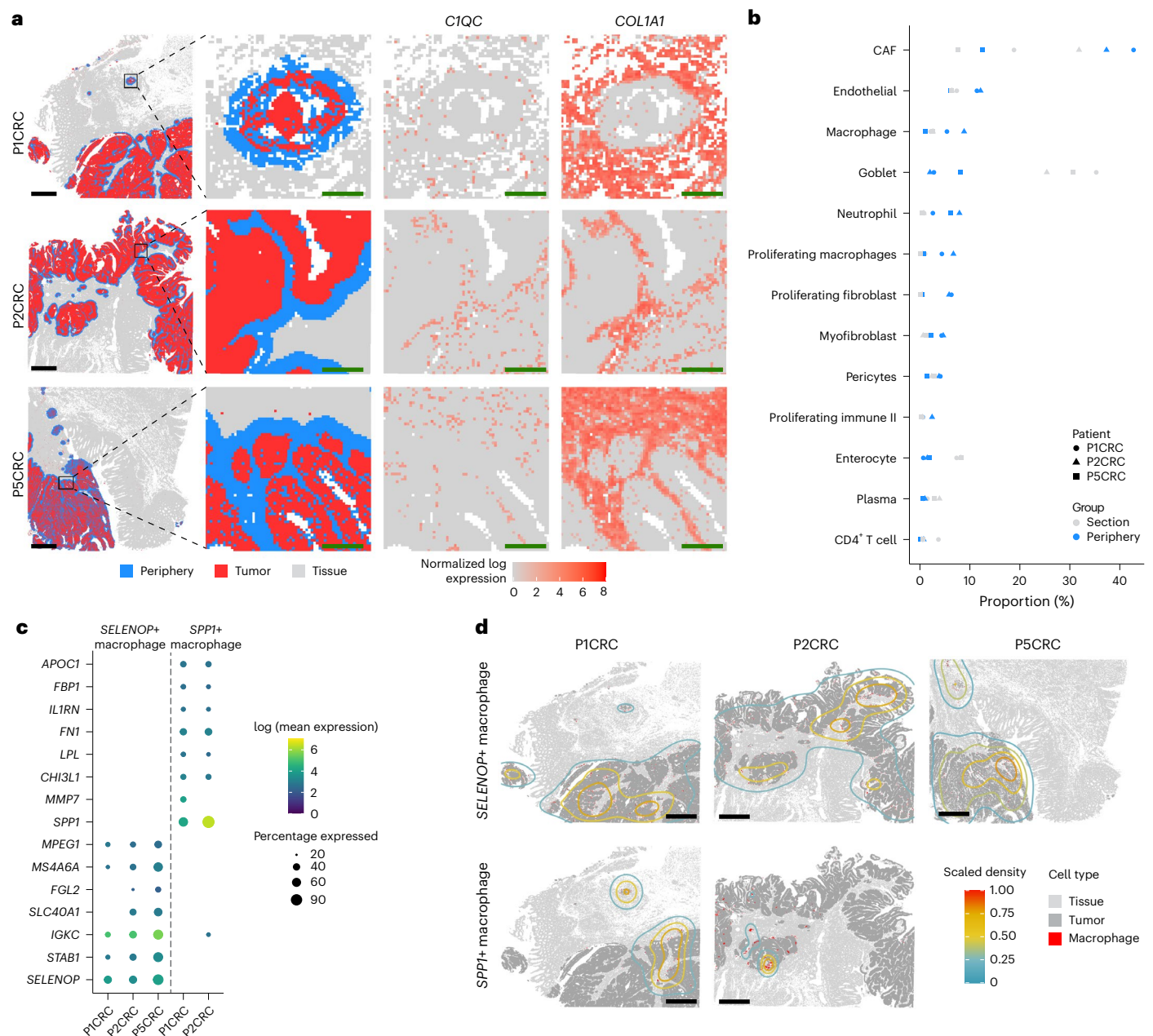


Fig. 4 | Cellular composition of the tumor periphery in each CRC section. **a**, Analysis of the tumor periphery. Bins (8 μm) annotated as tumor cells are shown in red, with bins within 50 μm of the tumor periphery shown in blue. Rows correspond to three different samples. The first column shows the 6.5 × 6.5-mm capture area, the second column shows the magnified view, the third column shows the corresponding expression of *C1QC* (macrophages), and the fourth column shows the corresponding expression of *COL1A1* (fibroblasts). **b**, Dot plot

with the proportion of cell types in the tumor periphery (blue) and the rest of the tissue section (gray) for the three different blocks. **c**, Dot plot showing expression profiles of two distinct macrophage subpopulations identified at the boundary in the tumor samples studied. Dots are shown if a gene is expressed in at least 20% of the cells of a given group. **d**, Kernel density maps showing the differential spatial localization of *SELENOP*⁺ and *SPP1*⁺ macrophages and how they are associated with tumor areas. Scale bars, 1 mm (black), 125 μm (green).

signaling pathways. Notably, the epithelial–mesenchymal transition pathway and complement system were upregulated in both macrophage subpopulations (Fig. 5a). Analysis of the tumor cells revealed that the different macrophage subpopulations were localized in tumor regions that also had distinct gene expression profiles. Tumor cells in areas enriched for *SPP1*⁺ macrophages showed differential expression of *TGFBI* and *PERP* genes (Fig. 5b), while tumor regions closer to *SELENOP*⁺ macrophages were enriched for *REG1A* and *REG1B* genes (patient P1CRC) or the *LCN2* gene (P2CRC and P5CRC; Fig. 5b). While *REG1A* and *REG1B* enrichment near *SELENOP*⁺ macrophages was primarily observed in P1CRC, we found upregulated expression of these genes

in P2CRC goblet cells within the *SELENOP*⁺ macrophage niche. Unsupervised clustering analysis of all goblet cells identified this distinct subpopulation (Fig. 5c). The goblet subpopulation expressing *REG1A* and *REG1B* localized at the normal–tumor tissue border of P1CRC and P2CRC, suggesting that these cells may be progressing to a tumorigenic state (Fig. 5d).

When we extended the characterization of macrophage diversity across the entire tissue sections, four distinct subpopulations became evident. *SPP1* expression was restricted to one of these subpopulations. *SELENOP* was expressed in the other three subpopulations, one of which also expressed *FOLR2*, albeit in a low proportion of the subpopulation.

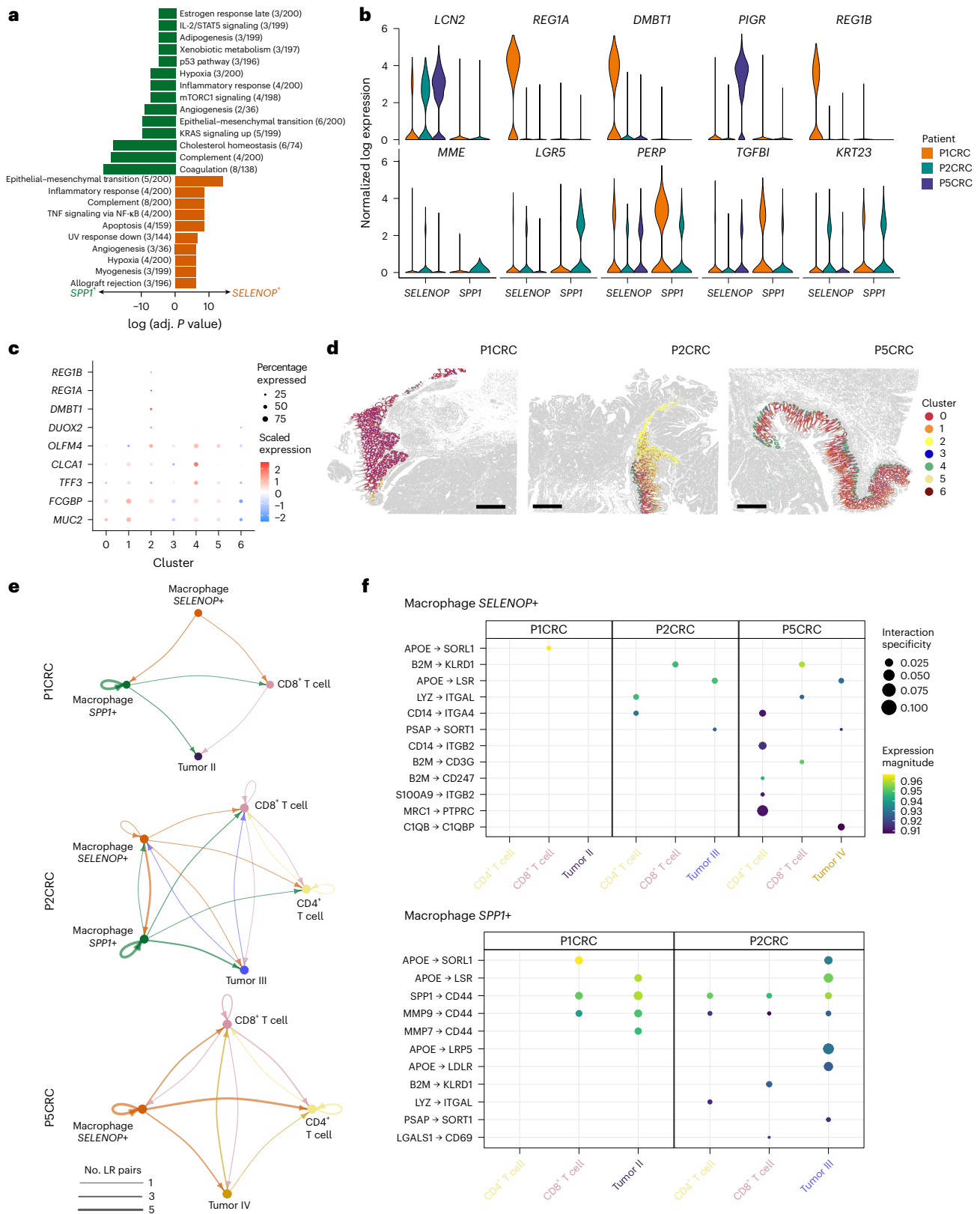


Fig. 5 | Identification and localization of two macrophage subpopulations in the TME. a, Bar plot showing the enriched gene sets for the macrophage subpopulations identified. The length of the bar represents the $-\log_{10}$ (adjusted *P* value) from one-tailed Fisher’s test. *P* values were corrected for multiple-hypothesis testing using the Benjamini–Hochberg method. Adj., adjusted; IL, interleukin; mTORC1, mechanistic target of rapamycin complex 1; STAT5, signal transducer and activator of transcription 5; UV, ultraviolet. **b**, Violin plots representing the expression of top genes in the tumor regions near *SPP1*⁺ (top)

and *SELENOP*⁺ (bottom) macrophages. **c**, Dot plot showing expression profiles of goblet cell subpopulations identified via unsupervised clustering. **d**, Spatial plots showing the localization of the identified goblet cell subpopulations. **e**, Interaction networks of macrophages, T cells and tumor cells in the boundary regions (50 μm). Nodes represent cell types, and edges represent the number of significant ligand–receptor (LR) pairs. **f**, Dot plot representing the expression and specificity of ligand–receptor pairs for *SPP1*⁺ and *SELENOP*⁺ macrophages as sources. Scale bars, 1 mm.

In line with previous reports³², the *FOLR2*+ macrophages, which were present only in one sample, were almost (>98%) exclusive to bins >50 μm from the tumor (Extended Data Fig. 7).

We next asked how the *SELENOP*+ and *SPPI*+ macrophages were interacting with the neighboring tumor cells and T cells. Using LIANA³³, we assessed cell–cell communication and inferred ligand–receptor interactions within the previously defined tumor periphery region ($\leq 50 \mu\text{m}$ of the tumor boundary). This revealed that the dominant *SPPI*+ macrophage interaction with tumor and T cells is via the CD44 receptor. *SELENOP*+ macrophages show distinct interactions with tumor cells and T cells, primarily influencing pro-tumor metabolic pathways and immune cell stimulation (Fig. 5e,f).

T cells exhibit clonally expanded niches within the CRC TME

It is known that T cell-infiltrated tumors have more positive patient outcomes than those with T cells excluded³⁴ and that the functional state of these infiltrated cells is also important³⁵. Thus, we explored the localization and function of T cells in our samples. Our periphery analysis identified T cells, but using the $8 \times 8\text{-}\mu\text{m}$ binned data meant that most T cells in the tumor periphery were assigned to doublet bins or rejected (the algorithm was unable to predict the cell type) and therefore excluded, making them challenging to localize (Fig. 6a and Extended Data Fig. 8). To mitigate this, we leveraged the $2 \times 2\text{-}\mu\text{m}$ data and assigned bins that were located within segmented nuclear polygons to create a gene-by-nucleus UMI count matrix for further processing (Fig. 6b). Using this approach, we identified T cells at the tumor boundary (Fig. 6c). We also examined the expression of known T cell markers (*TRAC* and *CD3E*) and other cell type markers, including *PECAMI* (endothelial), *IGKC* (plasma), *COL1A1* (CAF), *SPPI* or *SELENOP* (macrophages) and *CEACAM5* (tumor) (Extended Data Fig. 9) to obtain a fine-grained map of the cell types in these tissue areas. Through this analysis, we identified and localized both CD4^+ and CD8^+ T cells at the tumor periphery but not in the surrounding normal tissue, suggesting that these infiltrating lymphocytes may be playing an active anti-tumor role.

To validate findings from the Visium HD data, we profiled the samples using Xenium In Situ Gene Expression with cell segmentation staining. We first benchmarked the sensitivity of Xenium with Visium HD on our samples. We limited the Visium HD data to the 422 genes on the Xenium panel (Supplementary Table 2) and found that Xenium was $\sim 5.7\times$ more sensitive on a per-gene basis, while Visium HD captured $\sim 6.5\times$ more transcripts than Xenium owing to its whole-transcriptome nature (Extended Data Fig. 10). Consistent with the Visium HD findings, Xenium revealed heterogeneity within both tumor and macrophage cells (Fig. 7a,b). *SELENOP*+*STABI*+ macrophages were found near *REGIA*+*LCN2*+ tumor cells and goblet cells (Fig. 7c,d) while *SPPI*+ macrophages were localized near *TGFBI*+*PERP*+ tumor cells (Fig. 7e,f). Interestingly, we observed that CAFs, which localized at the border of the *TGFBI*+ tumor, also expressed *MMP11* (Fig. 7e,f), encoding a matrix metalloproteinase that breaks down ECM and is associated with poorer prognosis³⁶. This colocalization of *SPPI*+ macrophages, *TGFBI*+ tumor cells and *MMP11*+ CAFs within the TME may suggest a coordinated effort to promote tumorigenesis.

To better understand the T cell response, we explored the clonality of the antigen recognizing T cell receptors (TCRs) of the T cells in and around the CRC tumors. Using T cells isolated from dissociated tumor cells from the same patients, we performed Single Cell Immune Profiling to obtain the TCR sequences. This revealed a clonotype with 11% representation within the T cell population of sample P5CRC (TRAV38-1–TRAJ58; TRAB38-2/DV8–TRAJ57; TRBV4-2–TRBJ2-1; Supplementary Table 4) but no expansions in the other samples. No complementarity-determining region 3 (CDR3) matches to this clonotype were found in VDJdb (<https://vdjdb.cdr3.net/>), indicating that this clonotype recognizes a neoepitope specific to this tumor.

As expanded clonotypes indicate an active adaptive immune response, we sought to localize these cells within the tissue. We designed probes targeting the CDR3 regions of the expanded clonotype

and included them in the Xenium custom add-on panel (Supplementary Table 3). Xenium analysis identified clusters of clonally expanded CD8^+ T cells residing close to tumor cells and within gut-associated lymphoid tissues (Fig. 7g,h). These T cells were localized within *CXCL9*-, *CXCL10*- and *CXCL11*-expressing foci, where *STABI*+ macrophages, B cells and endothelial cells were present and contributing to the expression of these chemokines (Fig. 7h), known to recruit immune cells to the tumor site³⁷. This observation was validated in the corresponding region of the Visium HD data (Fig. 7i). *TRAC*+ T cells were identified near *CEACAM5*+ tumor cells, *SELENOP*+*C1QC*+ macrophages and *JCHAIN* B cells. *SELENOP* and *JCHAIN* were not included in the Xenium gene panel but were included in our analysis based on the Visium HD data, highlighting the complementary strengths of Xenium and Visium HD technologies.

Discussion

The advent of spatial transcriptomics has enabled a more comprehensive understanding of biology in health and disease and is particularly relevant in oncology, where the localization of specific cell types in the TME can have prognostic implications. By enabling precise mapping of the TME, these technologies reveal the complex spatial relationships among cells, which are crucial for understanding tumor progression and resistance to therapy. However, existing technologies have limitations related to resolution, tissue compatibility or ease of use. In this study, we introduced Visium HD, the next generation of the Visium technology, and used it to explore the TME in FFPE colon adenocarcinoma samples. We first demonstrated the high sensitivity, resolution and accuracy of Visium HD. Taking advantage of these features, we explored the immune cell composition in the immediate vicinity of CRC tumors, their potential role and interplay with other immune and tumor cells.

Immune cell interactions in the CRC TME remain poorly understood, with TAMs showing controversial roles due to mixed M1–M2 polarization and spatial distribution²⁶. For example, it has been hypothesized that tumor cells at the invasive front affect macrophage polarization²⁶. Visium HD enabled whole-transcriptome analysis within the spatially complex tumor boundary niche, with micrometer-level precision across a large tissue section, which has not been possible with existing technologies. We discovered macrophage populations with distinct gene expression profiles, unique spatial distributions and specific enriched pathways from data obtained from single archived tissue sections from different patients. Both *SPPI*+ and *SELENOP*+ macrophages are enriched in tumor tissues and more likely to adopt an M2-like phenotype exerting pro-tumor and pro-metastatic roles^{9,26,38,39}. In our samples, the spatial distribution of both macrophage subtypes and the upregulation of genes in known tumorigenic pathways⁴⁰ further support a pro-tumor role in the TME. *SPPI*+ macrophages were adjacent to tumor cells expressing *TGFBI* and *PERP*, and *SELENOP*+ macrophages were adjacent to tumor cells expressing *REGIA* and *LCN2* genes, all genes that have been associated with metastasis, advanced tumor stage and poor prognosis^{41–44}. Moreover, the predicted ligand–receptor communication between *SPPI*+ (via *SPPI*–*CD44*) and *SELENOP*+ (via *B2M*–*KLRD1*) macrophages with CD8^+ T cells in the TME could ultimately lead to reduced immune surveillance and evasion of the immune system by inhibiting cytotoxic activity^{45–47}. These data suggest different pro-tumor mechanisms exerted by macrophage populations in different TME niches.

While *REGIA* expression initially seemed exclusive to a particular set of tumor cells, a granular subclustering analysis of goblet cells revealed a distinct subpopulation expressing *REGIA*, with features of both goblet cells and *REGIA*+ tumor cells. While these *REGIA*+ cells exhibited reduced DGE of goblet cell markers, they exhibited higher DGE of *REGIA* tumor-associated features. These *REGIA*+ goblet cells likely represent a transitional state of tumorigenesis, as *REGIA* may be involved in early tumor development in CRC⁴⁸. Without Visium HD, identification and localization of this transitional goblet population would have been challenging.

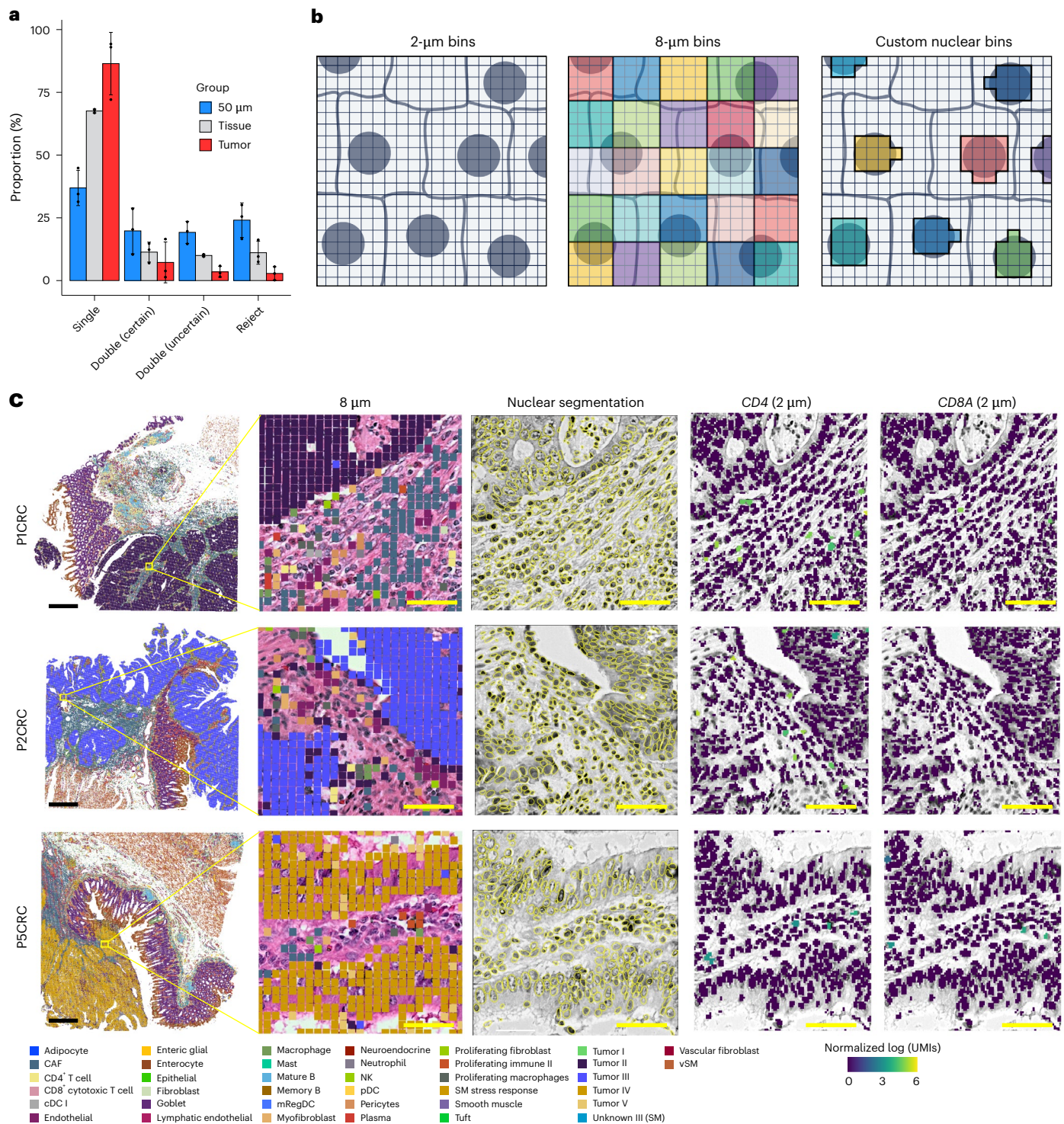


Fig. 6 | Spatial localization of T cells in the TME. a, Bar plot showing the proportion of each 8-µm bin class (single, double, rejected) for each tissue region for each patient ($n = 3$). Error bars represent mean values \pm s.d. **b**, Schematic representation of the two approaches for binning the 2×2 -µm barcoded squares in Visium HD data. The capture area of a Visium HD slide is a continuous grid of barcodes (left). The Space Ranger pipeline by default will create square bins (shown here as 8×8 -µm squares of a single color) that tile the entire tissue-containing capture area (middle). This is the cell assignment

method used for the 8×8 -µm binned data. An alternative is to use the nuclear stain from a high-resolution H&E microscope image to group together barcodes that underlie the same cell nuclei based on the 2×2 -µm data (right). **c**, Spatial plots showing a magnified view of regions with bins labeled by deconvolution results at 8 µm (left), nuclear segmentation results in the magnified regions (center) and normalized expression of *CD4* and *CD8A* (right) of the transformed UMI matrix by grouping 2×2 -µm bins within each of the segmented nuclei. Scale bars, 1 mm (black), 50 µm (yellow).

The pro-tumor features displayed by macrophage subpopulations and the potential role in inhibiting immune cell proliferation and function led us to further our analysis on the T cells near the tumors. T cell infiltration into CRC tumors has been associated with favorable

outcomes, suggesting a possible role for immunoeediting in controlling tumor growth³⁵. Using Xenium, we mapped the location of clonally expanded T cells within the CRC TME at single-cell resolution. These clonally expanded T cells colocalized with cells expressing *CXCL9*,

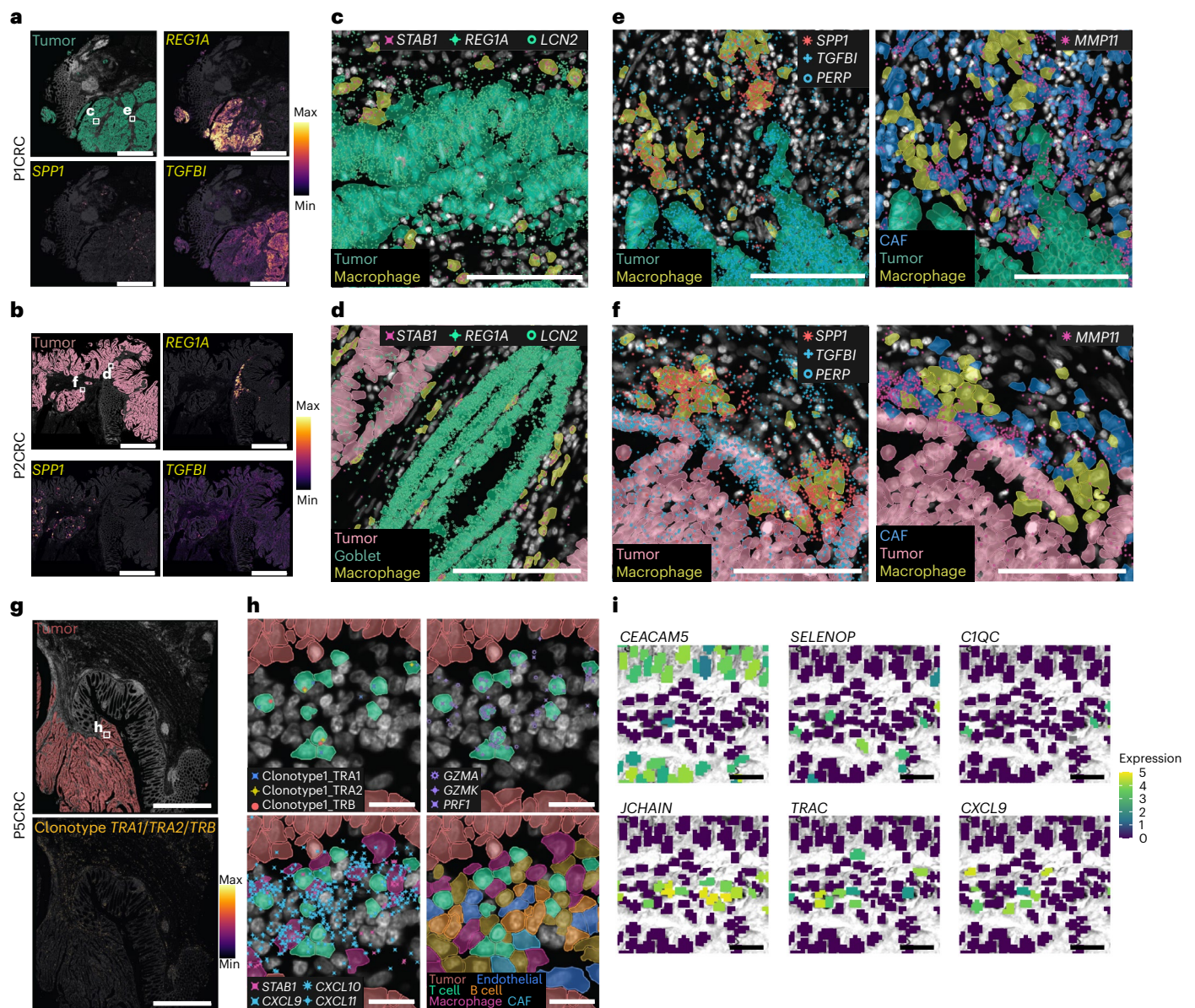


Fig. 7 | Xenium In Situ confirms the existence and localization of macrophage subtypes and clonally expanded T cells in the TME. a, b, Expression of *REG1A* and *TGFB1* transcripts (right) and *SPP1* (bottom left) within the tumor region (top left). Max, maximum; min, minimum. **c**, *STAB1*+ macrophages near *REG1A*+ and *LCN2*+ tumor cells. **d**, *STAB1*+ macrophages near *LCN2*+ tumor cells and *REG1A*+ and *LCN2*+ goblet cells. *STAB1* was used to visualize the macrophage subtype coexpressing *SELENOP*. **e, f**, *SPP1*+ macrophages shown in proximity of *TGFB1*+ and *PERP*+ tumor cells and *MMP11*+ CAFs. **g**, Combined expression of the

clonotype *TRA1/TRA2/TRB* in sample P5CRC. *TRA1*, *TRAV38-1-TRAJ58*; *TRA2*, *TRAB38-2/DV8-TRAJ57*; *TRB*, *TRBV4-2-TRBJ2-1*. **h**, Clonally expanded *CD8*⁺ T cells reside close to tumor cells and within *CXCL9*-, *CXCL10*- and *CXCL11*-expressing foci. **i**, Magnified view of the same regions using Visium HD with 2- μ m bins assigned to segmented nuclei. Bins are colored by the normalized log (UMI) counts of *CEACAM5*, *SELENOP*, *CIQC*, *JCHAIN*, *TRAC* and *CXCL9*. Scale bars, 2 mm in **a, b, g**; 100 μ m in **c, d–f**; 20 μ m in **h**; 50 μ m in **i**.

CXCL10 and *CXCL11*, encoding chemokines, which are known to attract cytotoxic T lymphocytes³⁷. Consistent with this finding, these expanded T cells expressed cytotoxic genes, including *PRF1*, *GZMA* and *GZMK*. Notably, macrophages within these regions emerged as the primary source of *CXCL9*, *CXCL10* and *CXCL11* expression. This finding suggests that, despite the overall immunosuppressive TME, there are niches of anti-tumor immune responses where T cells are actively recruited to the tumor boundary. This is an important observation, as the balance between the pro-tumor and anti-tumor macrophages influences tumor progression and therapy response. Further research into macrophage plasticity and their ability to switch between these states could provide potential targets for cancer management strategies^{49,50}. Identifying key biomarkers that signify this transition enables the development of new

therapeutic targets, which have the potential to allow for earlier-stage, targeted and personalized cancer treatments. A limitation of this study is the small sample size, preventing us from drawing broad conclusions. However, we demonstrate that high-resolution spatial technologies can provide comprehensive insights that will be key in identifying biomarkers as potential therapeutic targets for CRC. This study lays the groundwork for future breakthroughs using larger cohorts.

Future studies using more sophisticated analyses can take full advantage of the 2- μ m data afforded by Visium HD. While our nuclear segmentation analysis using the 2- μ m resolution data allowed us to locate T cells within the tumor boundaries, truly accurate cell type assignment requires advanced cell segmentation algorithms that are not yet available. This could be accomplished by either using cell

surface staining information or through the development of spatially aware methods capable of including information from neighboring bins during unsupervised clustering⁵¹. These methods would also account for small cells and cells in dense neighborhoods, mitigating any need for a single-cell reference dataset.

High-definition spatial technologies are providing increasingly detailed information into cancer biology. Our results exemplify the valuable insights gained from studying immune cell populations in the TME with high-definition, whole-transcriptome spatial technologies and pave the way for future research to improve our understanding of tumor evolution and to inform therapeutic advances. Our study combined whole-transcriptome and targeted in situ spatial technologies to obtain additional information on the TME heterogenic nature. Given the poor survival rates of many cancers, there is a pressing need for better diagnostic and prognostic biomarkers to inform clinical strategies.

Leveraging high-definition spatial technologies on large cohort studies to characterize cells in tumors, in combination with cutting-edge analytical approaches powered by machine learning and artificial intelligence, will yield a detailed appreciation of tumor heterogeneity and the cell-to-cell interactions in these different TME niches and the identification of spatially resolved biomarkers. This understanding will provide critical insights into tumor evolution and treatment resistance, guiding the identification of crucial biomarkers and the development of targeted therapies.

Online content

Any methods, additional references, Nature Portfolio reporting summaries, source data, extended data, supplementary information, acknowledgements, peer review information; details of author contributions and competing interests; and statements of data and code availability are available at <https://doi.org/10.1038/s41588-025-02193-3>.

References

- Xi, Y. & Xu, P. Global colorectal cancer burden in 2020 and projections to 2040. *Transl. Oncol.* **14**, 101174 (2021).
- Hossain, M. S. et al. Colorectal cancer: a review of carcinogenesis, global epidemiology, current challenges, risk factors, preventive and treatment strategies. *Cancers* **14**, 1732 (2022).
- O'Connell, J. B., Maggard, M. A. & Ko, C. Y. Colon cancer survival rates with the New American Joint Committee on Cancer sixth edition staging. *J. Natl Cancer Inst.* **96**, 1420–1425 (2004).
- Wang, W. et al. Molecular subtyping of colorectal cancer: recent progress, new challenges and emerging opportunities. *Semin. Cancer Biol.* **55**, 37–52 (2019).
- Guinney, J. et al. The consensus molecular subtypes of colorectal cancer. *Nat. Med.* **21**, 1350–1356 (2015).
- Singh, M. P., Rai, S., Pandey, A., Singh, N. K. & Srivastava, S. Molecular subtypes of colorectal cancer: an emerging therapeutic opportunity for personalized medicine. *Genes Dis.* **8**, 133–145 (2021).
- Sawayama, H., Miyamoto, Y., Ogawa, K., Yoshida, N. & Baba, H. Investigation of colorectal cancer in accordance with consensus molecular subtype classification. *Ann. Gastroenterol. Surg.* **4**, 528–539 (2020).
- Wen, R. et al. Single-cell sequencing technology in colorectal cancer: a new technology to disclose the tumor heterogeneity and target precise treatment. *Front. Immunol.* **14**, 1175343 (2023).
- Zhang, L. et al. Single-cell analyses inform mechanisms of myeloid-targeted therapies in colon cancer. *Cell* **181**, 442–459 (2020).
- Pelka, K. et al. Spatially organized multicellular immune hubs in human colorectal cancer. *Cell* **184**, 4734–4752 (2021).
- Becker, W. R. et al. Single-cell analyses define a continuum of cell state and composition changes in the malignant transformation of polyps to colorectal cancer. *Nat. Genet.* **54**, 985–995 (2022).
- Avraham-Davidi, I. et al. Spatially defined multicellular functional units in colorectal cancer revealed from single cell and spatial transcriptomics. *eLife* **14**, RP104815 (2025).
- Joanito, I. et al. Single-cell and bulk transcriptome sequencing identifies two epithelial tumor cell states and refines the consensus molecular classification of colorectal cancer. *Nat. Genet.* **54**, 963–975 (2022).
- Khaliq, A. M. et al. Refining colorectal cancer classification and clinical stratification through a single-cell atlas. *Genome Biol.* **23**, 113 (2022).
- Li, H. et al. Reference component analysis of single-cell transcriptomes elucidates cellular heterogeneity in human colorectal tumors. *Nat. Genet.* **49**, 708–718 (2017).
- Lee, H.-O. et al. Lineage-dependent gene expression programs influence the immune landscape of colorectal cancer. *Nat. Genet.* **52**, 594–603 (2020).
- Cho, C.-S. et al. Microscopic examination of spatial transcriptome using Seq-Scope. *Cell* **184**, 3559–3572 (2021).
- Poovathingal, S. et al. Nova-ST: nano-patterned ultra-dense platform for spatial transcriptomics. *Cell Rep. Methods* **4**, 100831 (2024).
- Schott, M. et al. Open-ST: high-resolution spatial transcriptomics in 3D. *Cell* **187**, 3953–3972 (2023).
- Vickovic, S. et al. High-definition spatial transcriptomics for in situ tissue profiling. *Nat. Methods* **16**, 987–990 (2019).
- Liu, Y. et al. High-spatial-resolution multi-omics sequencing via deterministic barcoding in tissue. *Cell* **183**, 1665–1681 (2020).
- Fu, X. et al. Polony gels enable amplifiable DNA stamping and spatial transcriptomics of chronic pain. *Cell* **185**, 4621–4633 (2022).
- Lee, Y. et al. XYSeq: spatially resolved single-cell RNA sequencing reveals expression heterogeneity in the tumor microenvironment. *Sci. Adv.* **7**, eabg4755 (2021).
- Peng, Z., Ye, M., Ding, H., Feng, Z. & Hu, K. Spatial transcriptomics atlas reveals the crosstalk between cancer-associated fibroblasts and tumor microenvironment components in colorectal cancer. *J. Transl. Med.* **20**, 302 (2022).
- Liu, H.-T. et al. Spatially resolved transcriptomics revealed local invasion-related genes in colorectal cancer. *Front. Oncol.* **13**, 1089090 (2023).
- Ozato, Y. et al. Spatial and single-cell transcriptomics decipher the cellular environment containing HLA-G⁺ cancer cells and SPP1⁺ macrophages in colorectal cancer. *Cell Rep.* **42**, 111929 (2023).
- Wang, F. et al. Single-cell and spatial transcriptome analysis reveals the cellular heterogeneity of liver metastatic colorectal cancer. *Sci. Adv.* **9**, eadf5464 (2023).
- Janesick, A. et al. High resolution mapping of the tumor microenvironment using integrated single-cell, spatial and in situ analysis. *Nat. Commun.* **14**, 8353 (2023).
- Tian, L., Chen, F. & Macosko, E. Z. The expanding vistas of spatial transcriptomics. *Nat. Biotechnol.* **41**, 773–782 (2023).
- Du, M. R. M. et al. Benchmarking spatial transcriptomics technologies with the multi-sample SpatialBenchVisium dataset. *Genome Biol.* **26**, 77 (2025).
- Dolan, B. & Hansson, G. C. Mucins. In *Encyclopedia of Cell Biology* 2nd edn (eds Bradshaw, R. A. et al.) 415–421 (Academic, 2023).
- Xun, Z. et al. Reconstruction of the tumor spatial microenvironment along the malignant-boundary–nonmalignant axis. *Nat. Commun.* **14**, 933 (2023).

33. Dimitrov, D. et al. LIANA+ provides an all-in-one framework for cell–cell communication inference. *Nat. Cell Biol.* **26**, 1613–1622 (2024).
34. Khalaf, K. et al. Aspects of the tumor microenvironment involved in immune resistance and drug resistance. *Front. Immunol.* **12**, 656364 (2021).
35. Yang, W. et al. T-cell infiltration and its regulatory mechanisms in cancers: insights at single-cell resolution. *J. Exp. Clin. Cancer Res.* **43**, 38 (2024).
36. Tian, X. et al. Expression of CD147 and matrix metalloproteinase-11 in colorectal cancer and their relationship to clinicopathological features. *J. Transl. Med.* **13**, 337 (2015).
37. Tokunaga, R. et al. CXCL9, CXCL10, CXCL11/CXCR3 axis for immune activation — a target for novel cancer therapy. *Cancer Treat. Rev.* **63**, 40–47 (2018).
38. Wu, L. et al. Cellular crosstalk of macrophages and therapeutic implications in non-small cell lung cancer revealed by integrative inference of single-cell transcriptomics. *Front. Pharmacol.* **14**, 1295442 (2023).
39. Qi, J. et al. Single-cell and spatial analysis reveal interaction of FAP⁺ fibroblasts and SPP1⁺ macrophages in colorectal cancer. *Nat. Commun.* **13**, 1742 (2022).
40. Liberzon, A. et al. The Molecular Signatures Database hallmark gene set collection. *Cell Syst.* **1**, 417–425 (2015).
41. Dasgupta, A. et al. Anticachectic regulator analysis reveals Perp-dependent antitumorigenic properties of 3-methyladenine in pancreatic cancer. *JCI Insight* **7**, e153842 (2022).
42. Santiago-Sánchez, G. S. et al. Biological functions and therapeutic potential of lipocalin 2 in cancer. *Int. J. Mol. Sci.* **21**, 4365 (2020).
43. Ma, C. et al. Extracellular matrix protein β ig-h3/TGFBI promotes metastasis of colon cancer by enhancing cell extravasation. *Genes Dev.* **22**, 308–321 (2008).
44. Zhou, M. et al. N⁶-methyladenosine modification of REG1 α facilitates colorectal cancer progression via β -catenin/MYC/LDHA axis mediated glycolytic reprogramming. *Cell Death Dis.* **14**, 557 (2023).
45. Eugène, J. et al. The inhibitory receptor CD94/NKG2A on CD8⁺ tumor-infiltrating lymphocytes in colorectal cancer: a promising new druggable immune checkpoint in the context of HLAE/ β 2m overexpression. *Mod. Pathol.* **33**, 468–482 (2020).
46. Abd Hamid, M. et al. Enriched HLA-E and CD94/NKG2A interaction limits antitumor CD8⁺ tumor-infiltrating T lymphocyte responses. *Cancer Immunol. Res.* **7**, 1293–1306 (2019).
47. Klement, J. D. et al. An osteopontin/CD44 immune checkpoint controls CD8⁺ T cell activation and tumor immune evasion. *J. Clin. Invest.* **128**, 5549–5560 (2018).
48. Astrosini, C. et al. REG1A expression is a prognostic marker in colorectal cancer and associated with peritoneal carcinomatosis. *Int. J. Cancer* **123**, 409–413 (2008).
49. Ganesh, K. et al. Immunotherapy in colorectal cancer: rationale, challenges and potential. *Nat. Rev. Gastroenterol. Hepatol.* **16**, 361–375 (2019).
50. Goossens, P. et al. Membrane cholesterol efflux drives tumor-associated macrophage reprogramming and tumor progression. *Cell Metab.* **29**, 1376–1389 (2019).
51. Si, Y. et al. FICTURE: scalable segmentation-free analysis of submicron-resolution spatial transcriptomics. *Nat. Methods* **21**, 1843–1854 (2024).

Publisher's note Springer Nature remains neutral with regard to jurisdictional claims in published maps and institutional affiliations.

Open Access This article is licensed under a Creative Commons Attribution-NonCommercial-NoDerivatives 4.0 International License, which permits any non-commercial use, sharing, distribution and reproduction in any medium or format, as long as you give appropriate credit to the original author(s) and the source, provide a link to the Creative Commons licence, and indicate if you modified the licensed material. You do not have permission under this licence to share adapted material derived from this article or parts of it. The images or other third party material in this article are included in the article's Creative Commons licence, unless indicated otherwise in a credit line to the material. If material is not included in the article's Creative Commons licence and your intended use is not permitted by statutory regulation or exceeds the permitted use, you will need to obtain permission directly from the copyright holder. To view a copy of this licence, visit <http://creativecommons.org/licenses/by-nc-nd/4.0/>.

© The Author(s) 2025

Visium HD Development Team

Michelli Faria de Oliveira¹, Juan Pablo Romero¹, Meii Chung^{1,2}, Stephen R. Williams¹, Andrew D. Gottscho¹, Anushka Gupta¹, Seayar Mohabbat¹, David J. Sukovich¹, David M. Patterson¹ & Sarah E. B. Taylor¹

A full list of members and their affiliations appears in the Supplementary Information.

Methods

Biomaterials

Human biological samples were obtained from Discovery Life Sciences. The research use of these specimens was approved by the corresponding institutional review boards under protocol numbers DLS-BB044-v.1 and SB-GP_v1. All patients provided written informed consent to Discovery Life Sciences for the research use of their biological samples.

An overview of the experimental design is presented in Fig. 1. Samples from five patients with colon adenocarcinoma (two males, three females, ages 58–72, pretreatment) were included in this study. From each patient, we included CRC FFPE blocks and NAT blocks for a subset of three patients (bringing the total to eight FFPE blocks), and we obtained paired freshly frozen dissociated tumor cells (for immune profiling analysis), alongside the three selected FFPE blocks used for spatial profiling (Table 1).

Tissue sectioning

Adjacent or near-adjacent 5- μ m sections were taken from the FFPE tissue blocks following the Xenium In Situ for FFPE – Tissue Preparation Guide (CG000578, revision C) for the Xenium workflow or the Visium CytAssist Spatial Gene Expression for FFPE – Tissue Preparation Guide (CG000518, revision C) for the Visium workflows.

Visium HD Spatial Gene Expression

H&E staining and imaging were performed following the Visium HD FFPE Tissue Preparation Handbook (CG000684). Samples were then processed and sequenced following the Visium HD Spatial Gene Expression Reagent Kits User Guide (CG000685). Space Ranger version 3.0 was used for analysis. In addition to the native 2- μ m feature size, Space Ranger outputs Visium HD data binned to 8- μ m and 16- μ m resolution. Unless otherwise specified, downstream analyses were performed on the 8- μ m resolution data, which provide a 16-fold increase in the average number of UMI reads per bin in the gene–barcode matrix compared to a 2- μ m square (Visium HD Spatial Gene Expression Performance Technical Note, CG000686, revision A), which is of a reasonable size to be processed through third-party tools. Additionally, the 8- μ m bin data provide robust cell type annotations (that is, bins are small enough to provide single-cell scale for most cell types). We merged the UMI count matrices of the three sections and, given the dataset's large size, we adopted the sketch-based analysis approach in Seurat (https://satijalab.org/seurat/articles/seurat5_sketch_analysis), sampling 15% of the entire dataset for downstream analysis^{52,53}. The 15% sampling rate was chosen to ensure efficient computational performance. We used the leverage score as the sketching method. This method oversamples rare populations to preserve the biological complexity of the sample. We identified variable features, scaled the data, performed principal-component (PC) analysis (PCA) and conducted graph-based clustering (20 PCs, resolution = 0.8). DGE analysis identified cluster marker genes, enabling manual annotation into ten broad cell types (level 1). For level 2 annotations, we reclustered each level 1 cluster (25 PCs, resolution = 0.1) to refine subtypes, performed DGE and annotated cell types. Final annotations were extended to the full dataset.

When needed, the 2 \times 2- μ m data were used (in combination with nuclear stain) to provide additional information, particularly to locate smaller cell types (Nuclear segmentation).

Spatial accuracy

To measure spatial accuracy of mRNA detection, we identified morphologically distinct ROIs and then pinpointed marker genes unique to each ROI. These marker genes should be expressed only in squares directly beneath their corresponding ROI. Using QuPath version 0.4.4 (ref. 54), we selected four ROIs within normal colon mucosal glands (hereafter referred to as 'source masks') and areas of adjacent muscularis mucosae ('adjacent masks'), choosing three goblet cell marker genes (*CLCA1*, *FCGBP* and *MUC2*). We mapped the locations of all transcripts

for these marker genes and calculated the proportion of accurately localized transcripts for each of the four ROIs. For the remaining transcripts, we determined the Euclidean distance from the edge of the nearest source mask to the square of transcript detection. Additionally, we calculated the densities of the marker genes within both the source and adjacent masks for each ROI.

Visium CytAssist Spatial Gene Expression for FFPE

Visium CytAssist Spatial Gene Expression for FFPE ('Visium v2') was run on a subset of samples to demonstrate technological improvements of Visium HD. FFPE serial sections (5 μ m) were placed on standard glass slides and stained with H&E following the Demonstrated Protocol Visium CytAssist Spatial Gene Expression for FFPE – Deparaffinization, H&E Staining, Imaging & Decrosslinking (CG000520). Samples were processed and sequenced following the Visium CytAssist Spatial Gene Expression Reagent Kits User Guide (CG000495). Space Ranger version 3.0 was used for analysis.

Sensitivity comparison of Visium v2 and Visium HD

We assessed the sensitivity of Visium HD compared to Visium v2 on a gene-by-gene basis. Matched areas were manually selected in Loupe Browser version 8.0, and probe–barcode matrices from each dataset, generated by Space Ranger, were imported into Seurat version 5 (ref. 52) using the `read10xh5()` function. We used the `ggplot2R` package to graph per-probe UMI counts. The data were displayed on a $\log_{10} + 1$ scale, with Spearman correlations calculated as r^2 . Our comparison spanned all probes across the entire transcriptome and specifically focused on probes crossing an exon–exon splice junction (7,605 of 54,580 probes). This latter comparison helps exclude most probes that could target gDNA or be susceptible to off-target effects. These probes that are marked as potentially binding to gDNA were excluded from the analysis computationally.

The gDNA estimate is obtained by fitting a piecewise linear model to genes with both spliced and unspliced probes. The model predicts the log-transformed gene counts for unspliced probes as a function of log-transformed gene counts for spliced probes and log-transformed estimated gDNA counts per gene per 1,000 spots under tissue:

$$x_{\text{unspliced}} = \text{gDNA} + B(x_{\text{spliced}}) - \hat{x}_{\text{gDNA}} \mathbb{I}(x_{\text{spliced}} > \hat{x}_{\text{gDNA}}),$$

where \hat{x}_{gDNA} is the estimated gDNA UMIs per gene, $x_{\text{unspliced}}$ and x_{spliced} are the average number of UMIs corresponding to unspliced and spliced probes from a single gene, respectively, and $\mathbb{I}(x_{\text{spliced}} > \hat{x}_{\text{gDNA}})$ is an indicator function that equals one if x_{spliced} is greater than \hat{x}_{gDNA} and zero otherwise.

For any fixed estimate of \hat{x}_{gDNA} , the model parameters gDNA and B are estimated by fitting a linear regression with a two-dimensional parameter vector. The relevant \hat{x}_{gDNA} values to consider while fitting the model are only those x_{spliced} values seen in the genes under consideration. Therefore, a linear model with every x_{spliced} value seen in the dataset as \hat{x}_{gDNA} is fit, and the model with the smallest residual sum of squares is used for the estimates. For more details on gDNA, see the technical note Visium CytAssist Spatial Gene Expression for FFPE: Robust Data Analysis with Minimal Impact of Genomic DNA (CG000605, revision A).

Chromium Single Cell Gene Expression Flex

Cells were dissociated from 50- μ m FFPE curls using the Demonstrated Protocol for Isolation of Cells from FFPE Tissue Sections for Chromium Fixed RNA Profiling (CG000632). Library preparation and sequencing followed the Chromium Fixed RNA Profiling for Multiplexed Samples User Guide (CG000527, revision D). Cell Ranger version 8.0.0 was used for analysis. To build the atlas, we used Seurat version 5 (ref. 52) to import the H5 file produced by the `cellranger aggr` pipeline. We then plotted the distribution of UMIs and genes per barcode, excluding the top and

bottom 2.5% of the distribution to account for outliers. We then used the same sketch approach as the HD data: identified variable features, scaled the data, performed PCA and conducted graph-based clustering (25 PCs, resolution = 0.6) and performed DGE analysis to identify cluster marker genes, enabling manual annotation into ten broad cell types (level 1). For level 2 annotations, we reclustered each level 1 cluster (25 PCs, resolution = 0.1) to refine subtypes, performed DGE and annotated cell types. Final annotations were extended to the full dataset.

Spot deconvolution

Deconvolution methods aim to identify the cell types and their relative proportions contributing to the signal captured in a specific area (spot, square or bin). Spot deconvolution was used to classify and label bins with cell types derived from the Single Cell Atlas. We ran *spaceXr*⁵⁵ using doublet mode, which assigns one to two cell types per spot and is recommended for technologies with high spatial resolution such as Visium HD. Among the outputs, this mode provides the top two ranked cell types per spot, a matrix with the weights for all cell types in the reference in each of the spots and a variable representing the class of every bin. The available classes are 'singlet' (one cell type), 'doublet_certain' (two cell types), 'doublet_uncertain' (two cell types, but only confident of one), 'reject' (no prediction given). See the *spaceXr* vignette for more detail (<https://raw.githubusercontent.com/dmccable/spaceXr/master/vignettes/spatial-transcriptomics.html>). Owing to the increased number of barcoded squares in Visium HD, we modified the code to improve runtime (<https://github.com/dmccable/spaceXr/pull/206>). We selected a minimum UMI threshold of 100 for a bin to be considered for the deconvolution step.

Characterizing the tumor periphery

To identify and analyze tumor periphery regions, we developed a custom pipeline (https://github.com/10XGenomics/HumanColonCancer_VisiumHD). The key advantage of this method is its versatility; it is not restricted to tumors and can be applied to identify cell types in the boundaries of other tissues, such as colon glands or skeletal muscle tissue. Our algorithm first selects all bins labeled with the given cluster or cell type. For each bin, the algorithm then identifies all neighboring bins within a user-defined radius. We defined this as 50 μm based on biological relevance and to exploit the high resolution of Visium HD. A 50- μm boundary analysis is not possible with Visium v2, which has a spot diameter of 55 μm . To accurately delineate the boundary of the cluster or cell type, the algorithm excludes bins with the same label as the initial bin. To further refine the boundary identification, we removed singlet bins labeled with the given cluster but not in proximity to other bins with the same label. Specifically, we excluded bins that had fewer than 25 neighboring bins with the same label to ensure the selection of well-defined regions within the tissue.

For the macrophage-specific analysis, we selected 8- μm bins that were deconvolved as macrophages and located within 50 μm of tumor regions. For each patient, variable features were identified, the data were scaled and PCA was performed. Graph-based clustering was then conducted using the top ten PCs with a resolution of 0.2. Clusters were annotated based on the expression of *SPPI* and *SELENO*P, and an integrated dataset was generated, including only the macrophage subpopulations consistently identified across all sections. To extend this analysis, all bins labeled as macrophages across all sections were included, irrespective of their proximity to the tumor boundary. For this broader dataset, 15 PCs and a resolution of 0.2 were used for clustering to achieve greater resolving power across patients. This approach aimed to determine whether the identified subpopulations were shared across patients or specific to individual patients.

Distance, local and regional analysis

After identifying regions enriched with immune cells, we selected the top three regions exhibiting the highest macrophage density (within

bins categorized as tumor tissue) and delineated these areas as ROIs with a radius of 350 μm . Additionally, we identified a 'cold' region lacking immune infiltration. To identify genes associated with elevated immune cell density, we used DGE analysis. Subsequent enrichment analysis of differentially expressed genes (ranked by \log_2 (fold change)) used the Hallmark gene sets linked to specific biological pathways⁴⁰ (<https://www.gsea-msigdb.org/gsea/msigdb/human/genesets.jsp?collection=H>).

Ligand–receptor analysis

To assess cell–cell communication between macrophages and T cells, we used LIANA version 0.1.12, which provides a framework to combine cell communication methods to infer ligand–receptor interactions³³. We selected all bins within the previously defined tumor periphery region (within 50 μm of the tumor boundary) to create an independent Seurat object to be used as input. We filtered the predicted interactions by selecting any interaction with $\text{aggregate_rank} \leq 0.01$. This procedure was done on a per-patient basis.

Immune density analysis

To map the locations of specific immune cell types in the CRC samples, we used the coordinates for each bin and their labels provided by deconvolution. We counted only bins that were labeled as singlets. We used 2D kernel density estimation to select regions enriched in a given cell type. Density values were scaled to a maximum of 1.

Nuclear segmentation

Using the 8 \times 8- μm binned data for the periphery analysis meant that most T cells in the tumor periphery were assigned to doublet bins or rejected (the algorithm was unable to predict the cell type) and therefore excluded, making them challenging to spatially localize (Fig. 6a and Extended Data Fig. 8). This is an effect of the 8 \times 8- μm binned data approach for cell assignment (Fig. 6b), in which smaller cell types such as T cells (as compared to tumor cells) may colocalize other cell types within the 8 \times 8- μm bin. To overcome this, we used an alternative approach to assign 2 \times 2- μm squares to cells. We first identified regions enriched in either CD4⁺ or CD8⁺ T cells, independent of whether they were assigned to a singlet or doublet bin, and, with the use of the nuclear stain from a high-resolution H&E microscope image, we performed nuclear segmentation on these regions. To segment nuclei from the H&E images and assign 2 \times 2- μm bins to the identified nuclei, we followed the analysis guide 'Nuclei Segmentation and Custom Binning of Visium HD Gene Expression Data' (<https://www.10xgenomics.com/analysis-guides/segmentation-visium-hd>). The segmentation procedure was run on the full section using StarDist⁵⁶. We used affine transformations to preserve the segmentation polygons when subsampling the image to specific ROIs. Once the 2- μm bins were assigned to the corresponding nuclear polygons, the data were transformed to create a gene-by-nucleus UMI count matrix for further processing.

Single-cell immune profiling

Freshly frozen dissociated tumor cells were sorted based on CD45 and CD3 expression to isolate T cells. Gene expression (5') and TCR libraries were generated and sequenced following the Chromium Next GEM Single Cell 5' Reagent Kits v2 (Dual Index) User Guide (CG000331). Cell Ranger version 8.0.0 was used for analysis.

Design of TCR clonotype probes

Custom probes for Xenium were developed to target three CDR3 sequences identified by VDJ sequencing (full list of clonotypes in Supplementary Table 4, probe sequences in Supplementary Table 3). One 40-bp probe was designed for each CDR3, centered on the CDR3 with some overhang into the adjacent framework regions. These probes were designed following the specifications in the Species Standalone Custom and Advanced Custom Panel Design for Xenium In Situ Technical Note (CG000683, revision C).

Xenium In Situ

The PICRC, P2CRC and P5CRC samples were processed following the Xenium In Situ Gene Expression with Morphology-based Cell Segmentation Staining User Guide (CG000749) with the Xenium Human Colon Gene Expression Panel (322 genes) supplemented with an additional 100 genes chosen to identify diverse immune populations we observed in the Visium HD data and characterize the TME (for the complete gene list, see Supplementary Table 2). The panel was designed using Xenium Panel Designer following the guidance in the Xenium Add-on Panel Design Technical Note (CG000643, revision B). The Xenium Onboard Analysis pipeline version 2.0.0 was run directly on the instrument for image processing, cell segmentation, image registration, decoding, deduplication and secondary analysis.

Reporting summary

Further information on research design is available in the Nature Portfolio Reporting Summary linked to this article.

Data availability

All datasets are available for download at the following website: <https://www.10xgenomics.com/products/visium-hd-spatial-gene-expression/dataset-human-crc>. Raw data have also been deposited in the Gene Expression Omnibus under accession number GSE280318. The source data used to generate most of the figures are provided as source data. For cases where the required source data contain more than 100,000 observations, the data are available for download as Parquet files at https://github.com/10XGenomics/HumanColonCancer_VisiumHD/tree/main/MetaData. Source data are provided with this paper.

Code availability

Custom scripts used for this paper are available on GitHub at https://github.com/10XGenomics/HumanColonCancer_VisiumHD. All code has also been deposited at Zenodo⁵⁷ (<https://zenodo.org/records/15042463>).

References

- Hao, Y. et al. Dictionary learning for integrative, multimodal and scalable single-cell analysis. *Nat. Biotechnol.* **42**, 293–304 (2024).
- Hie, B., Cho, H., DeMeo, B., Bryson, B. & Berger, B. Geometric sketching compactly summarizes the single-cell transcriptomic landscape. *Cell Syst.* **8**, 483–493 (2019).
- Bankhead, P. et al. QuPath: open source software for digital pathology image analysis. *Sci. Rep.* **7**, 16878 (2017).

- Cable, D. M. et al. Robust decomposition of cell type mixtures in spatial transcriptomics. *Nat. Biotechnol.* **40**, 517–526 (2022).
- Weigert, M. & Schmidt, U. Nuclei instance segmentation and classification in histopathology images with StarDist. In *2022 IEEE International Symposium on Biomedical Imaging Challenges (ISBIC)* 1–4 (IEEE, 2022).
- Oliveira, M. F. et al. High definition spatial transcriptomic profiling of immune cell populations in colorectal cancer. *Zenodo* <https://doi.org/10.5281/zenodo.15042463> (2025).

Acknowledgements

We thank the Visium HD Development Team who built the Visium HD Spatial Gene Expression product used in this study and the 10x Leadership Team for their support in this work. We also thank the members of the 10x Genomics microscopy, flow, sequencing and histopathology core facilities.

Author contributions

M.F.d.O., J.P.R. and S.E.B.T. conceived the study; M.F.d.O., M.C., A.D.G., S.E.P., S.M., N.R., D.J.S. and D.M.P. performed experiments; M.F.d.O., J.P.R., M.C., S.R.W. and S.E.B.T. analyzed and interpreted data; M.F.d.O., J.P.R., M.C., A.D.G. and S.E.B.T. wrote the manuscript.

Competing interests

All authors are current or former employees or shareholders of 10x Genomics.

Additional information

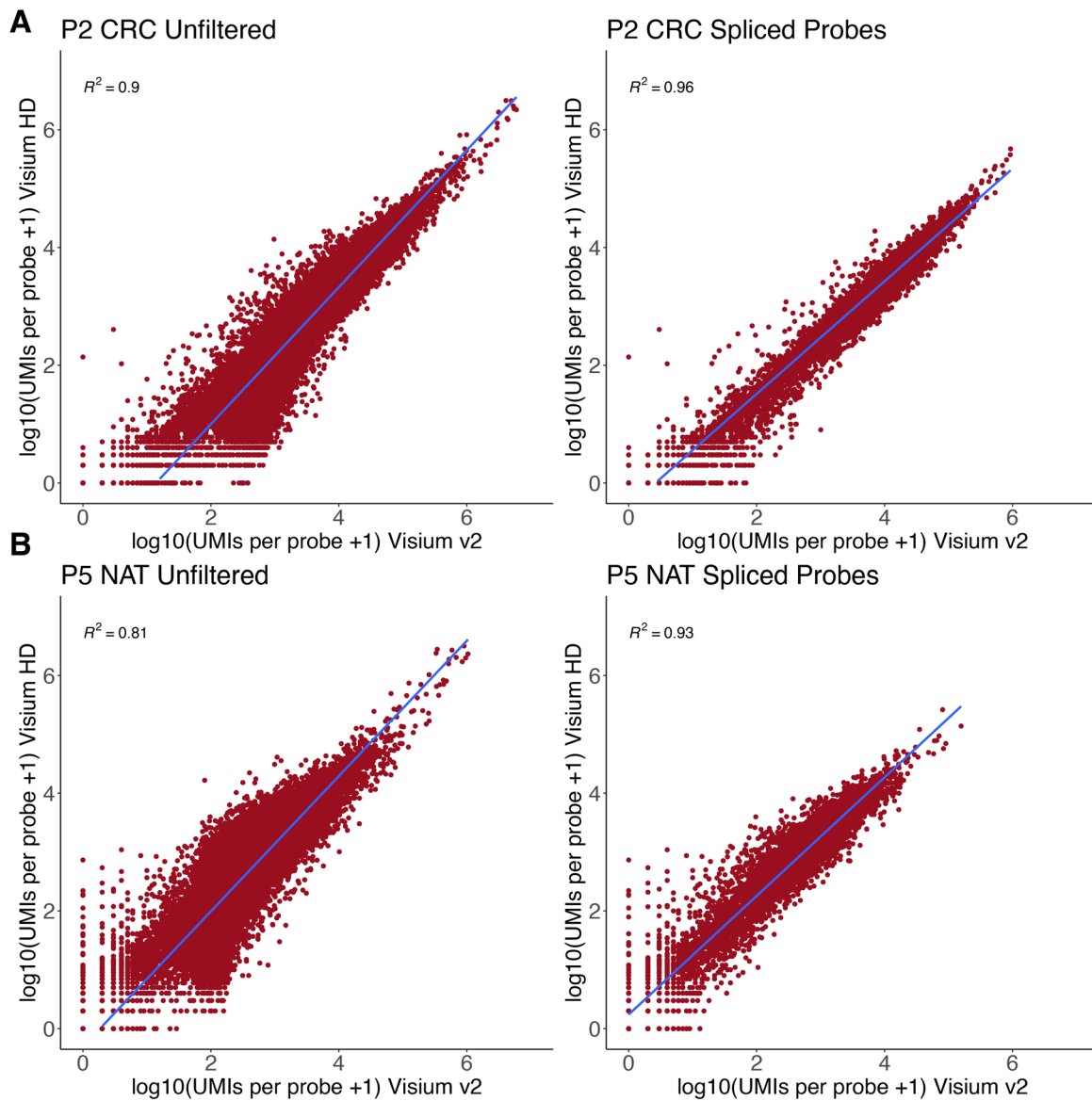
Extended data is available for this paper at <https://doi.org/10.1038/s41588-025-02193-3>.

Supplementary information The online version contains supplementary material available at <https://doi.org/10.1038/s41588-025-02193-3>.

Correspondence and requests for materials should be addressed to Sarah E. B. Taylor.

Peer review information *Nature Genetics* thanks Youqiong Ye, Fangqing Zhao, and Eduardo Villablanca for their contribution to the peer review of this work. Peer reviewer reports are available.

Reprints and permissions information is available at www.nature.com/reprints.

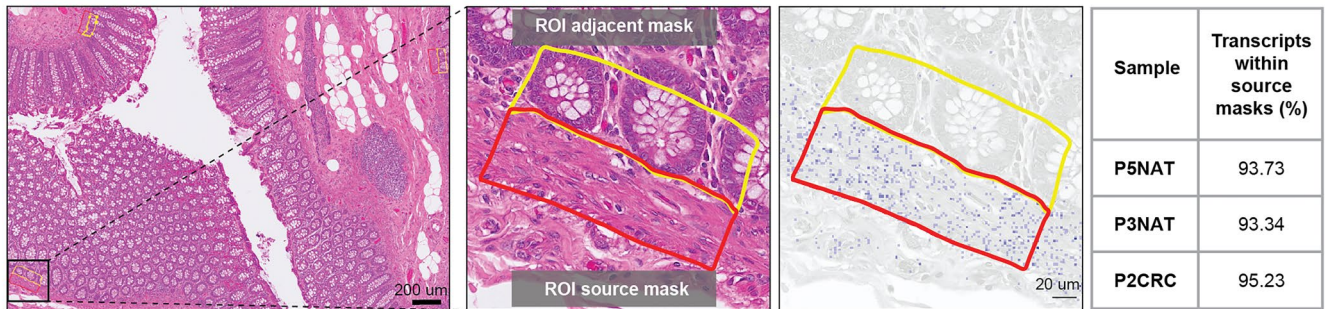


Extended Data Fig. 1 | Sensitivity comparisons between Visium v2 and Visium HD performed on serial sections of normal and colon cancer samples.

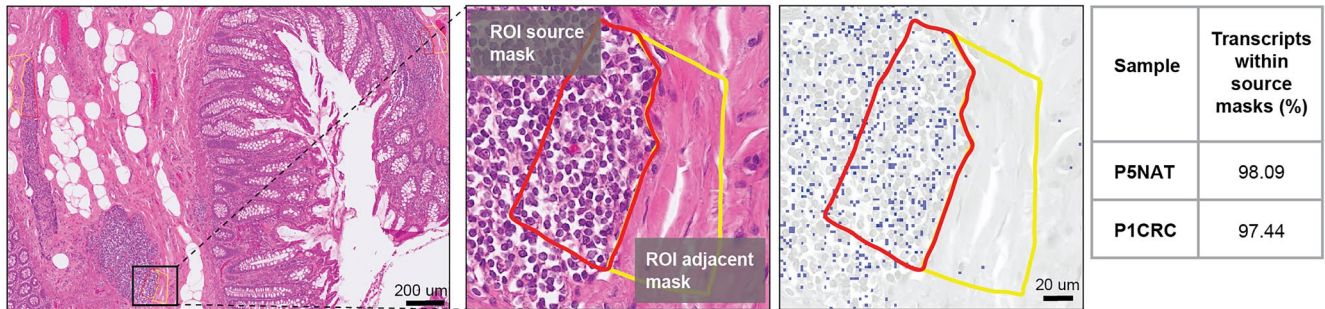
a. CRC sample (P2CRC). **b.** Normal colon mucosa sample (P5NAT). Comparisons show strong correlation between UMI counts from all probes (54,580 probes;

left panels, Unfiltered), and the probes that only span spliced gene target regions (7,605 probes; right panels, Spliced Probes), obtained from each assay, highlighting comparable sensitivity between assays.

A

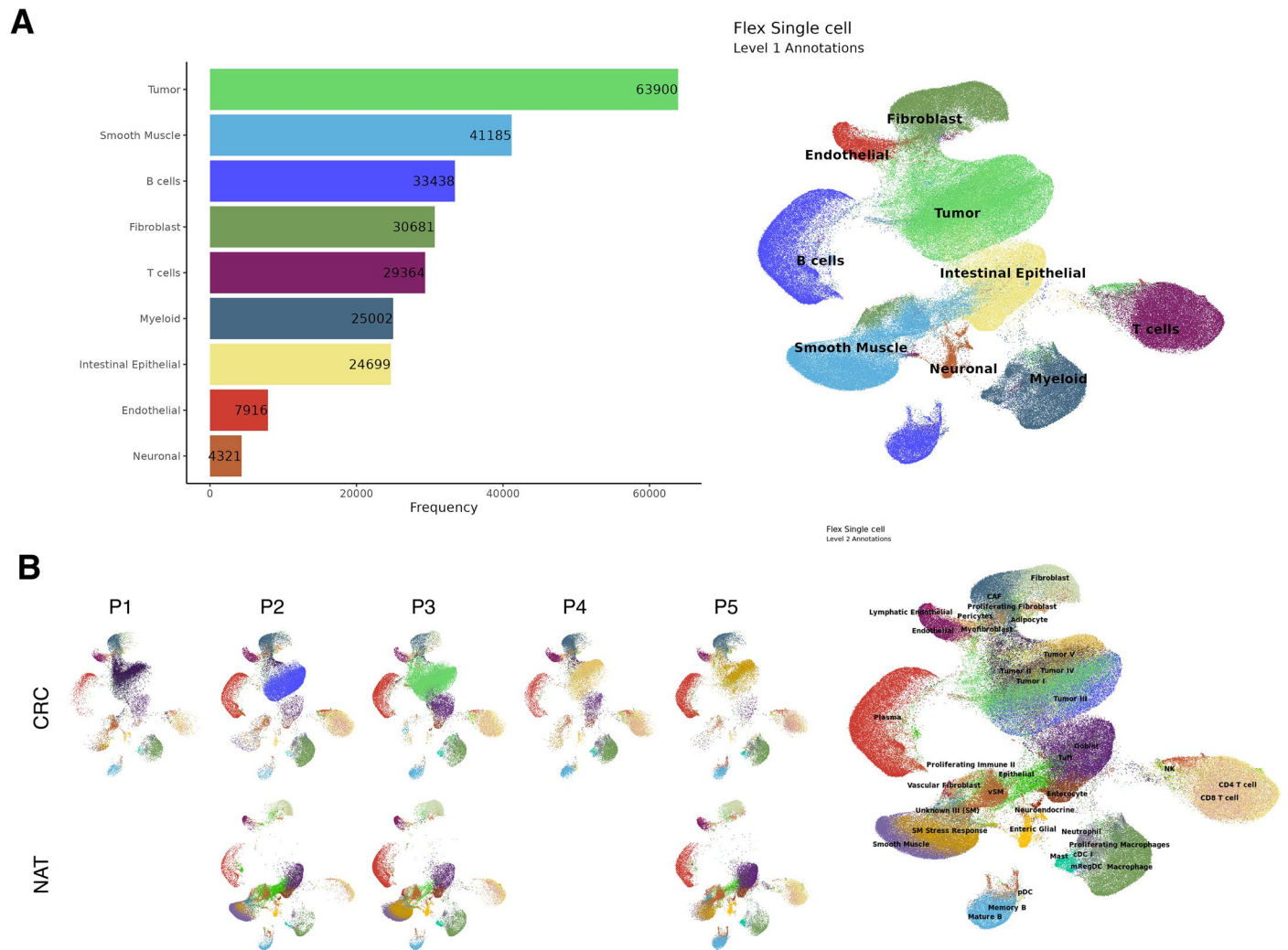


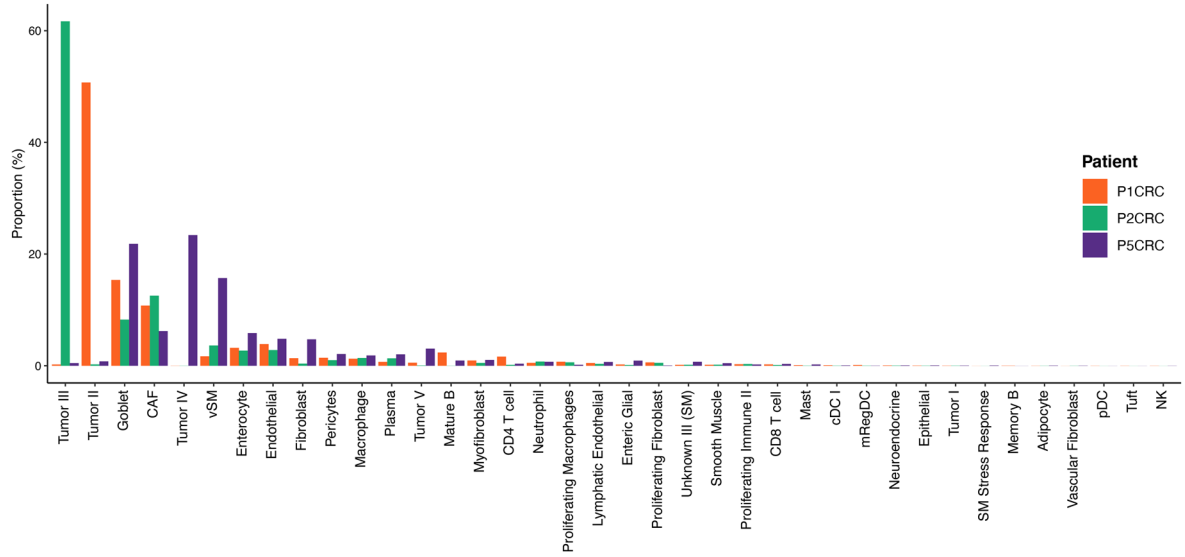
B



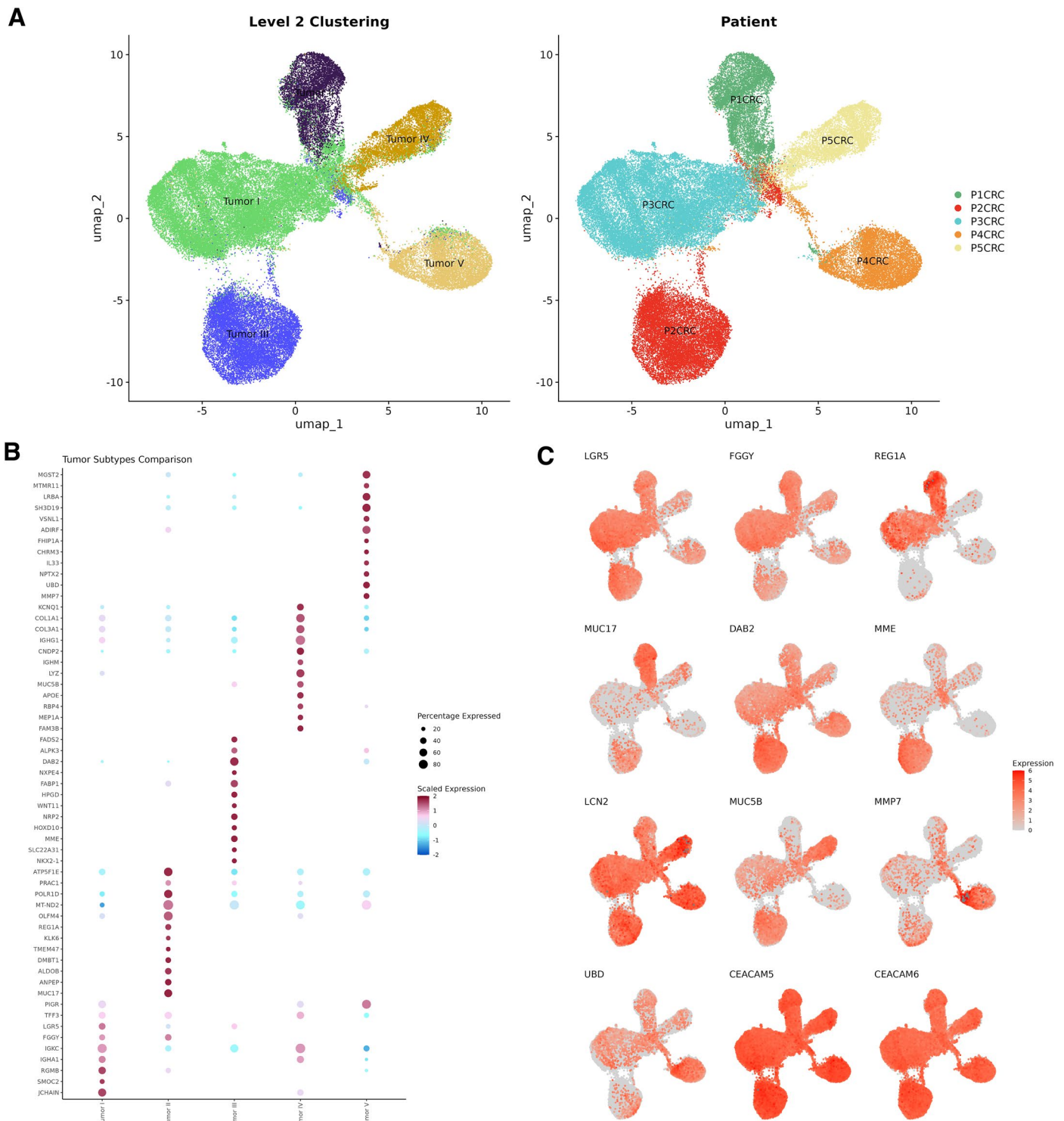
Extended Data Fig. 2 | Transcript localization accuracy. **a.** To assess localization accuracy of selected muscularis mucosae marker genes (*ACTA2*, *DES*, *GREM1*), we selected three regions of interest (ROIs) for each tissue; source masks (red) are muscularis mucosae, adjacent masks (yellow) are the immediately adjacent mucosa regions. The images show selected ROIs in a representative normal sample P5NAT. The table shows the median percentage of localized transcripts in the source in $n=3$ samples (one replicate per sample). **b.** We analyzed the

transcript localization of selected genes (*MS4AI*, *CDS2*, *CXCR4*) known to be enriched in immune cells within lymphoid regions in three ROIs. Source masks (red) are lymphoid regions, and adjacent masks (yellow) represent the immediately adjacent submucosa areas. The images show selected ROIs in a representative normal sample P5NAT. Table shows the median percentage of localized transcripts in the source in $n=3$ samples (one replicate per sample).



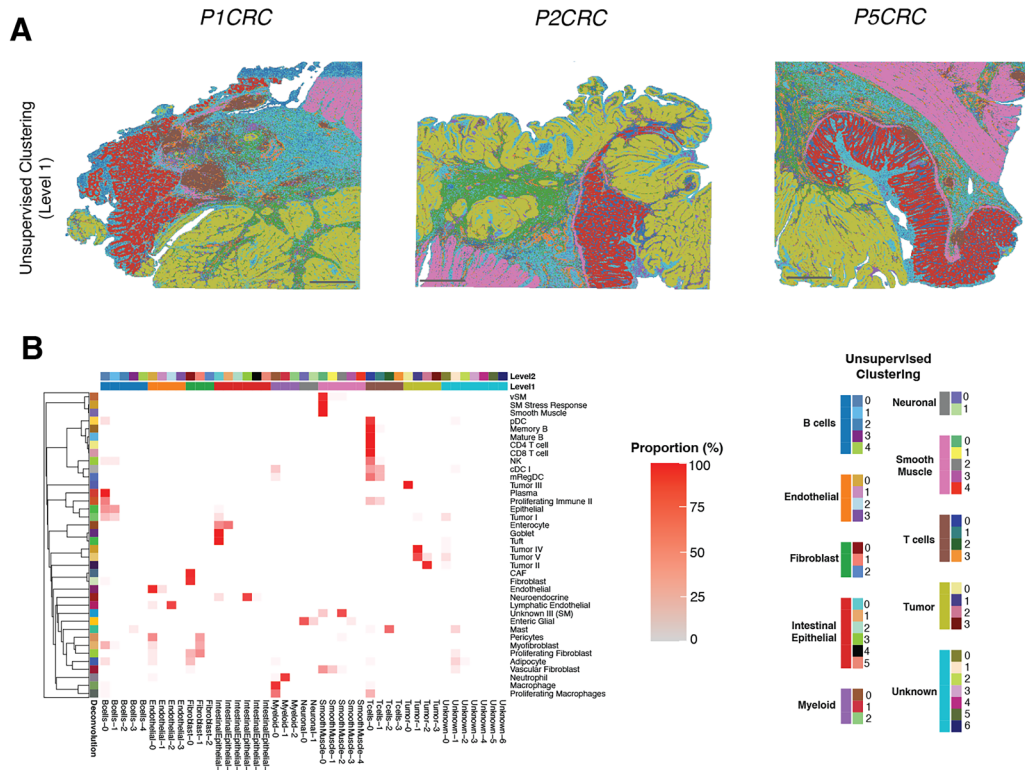


Extended Data Fig. 4 | Proportion of cell types identified in three CRC samples. Barplot with the proportion of each of the identified cell types after deconvolution on the three different CRC samples. Colors represent the sample.



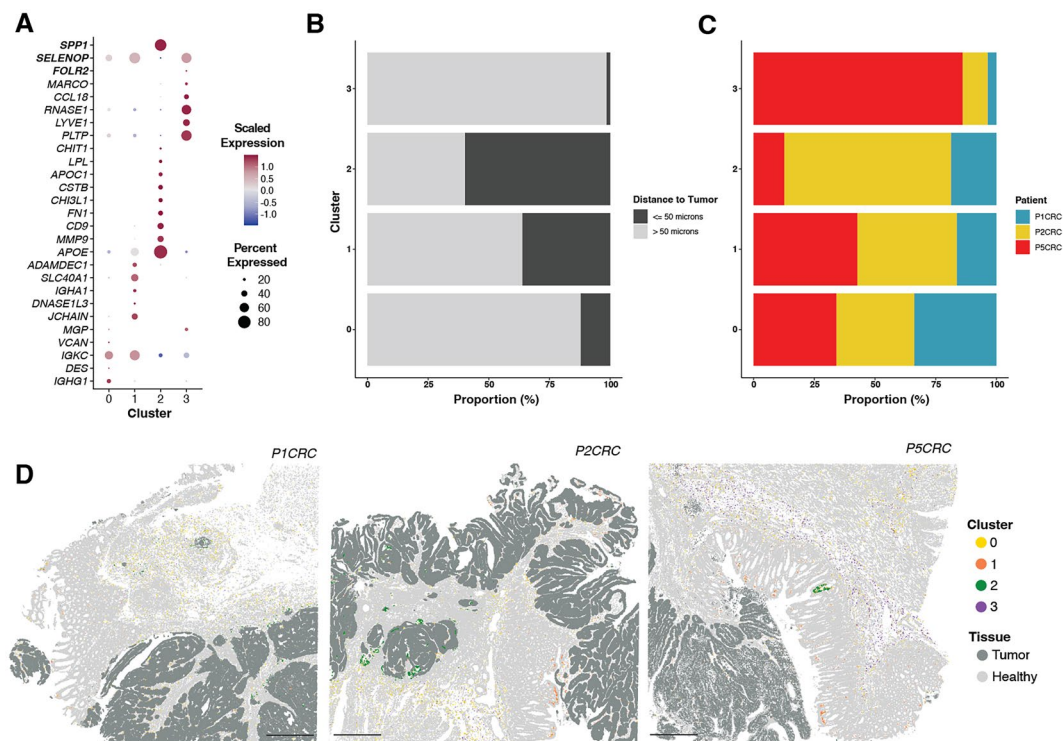
Extended Data Fig. 5 | Single cell analysis of tumor subpopulations in CRC (n=5) samples reveal tumor heterogeneity. a. UMAP plot with tumor cells colored by cluster (left) and colored by sample identifier (right). **b.** Dot plot

displaying the scaled expression of the top differentially expressed genes across the 5 tumor subpopulations. **c.** UMAP plot colored by log normalized UMI counts of differentially expressed genes and tumor markers (*CEACAM5*, *CEACAM6*).



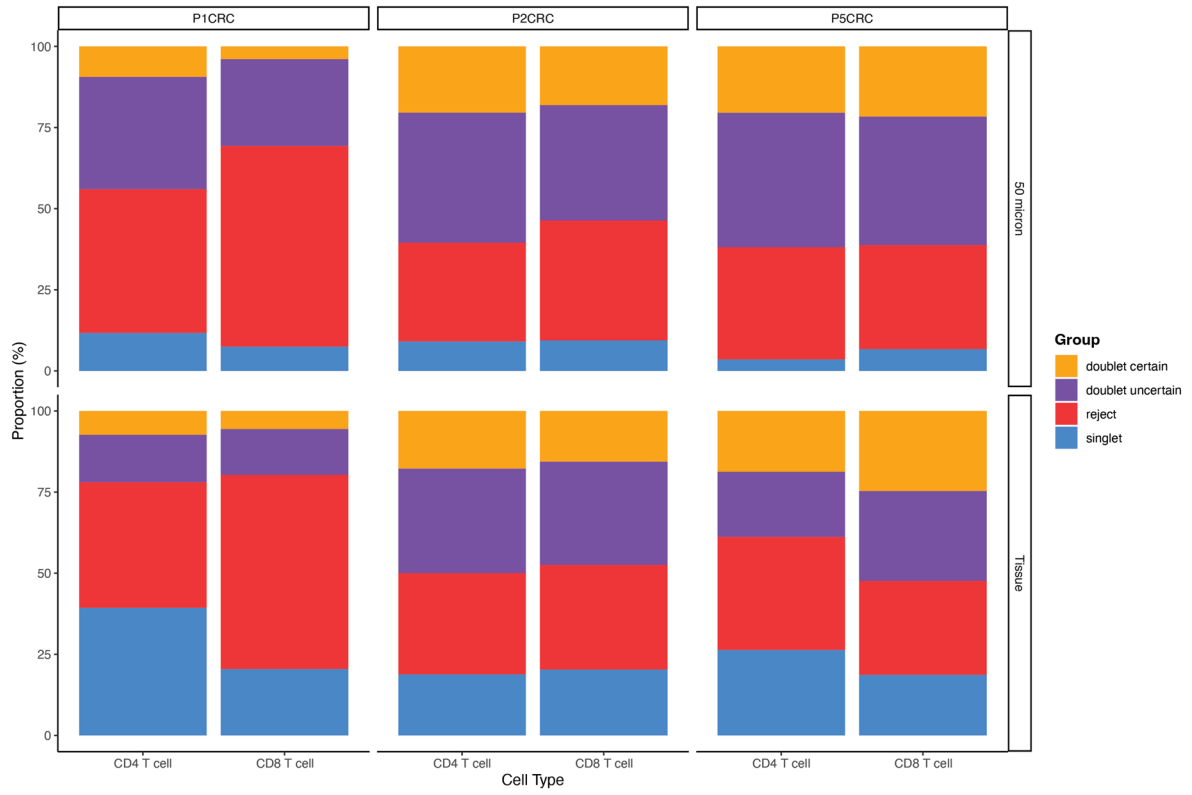
Extended Data Fig. 6 | Sketch based analysis of Visium HD data without the integration of single cell data. a. Spatial plots with bins colored by cell type identified level 1 unsupervised clustering. Scale bar = 1mm. **b.** Heatmap from confusion matrix showing the relationship between cell labels provided via

deconvolution (rows) and unsupervised clusters (columns). Heatmap is scaled by row, summing up to 100% per row. Longer color bars represent level 1 cell type annotations and small colored squares represent the level 2 clusters identified for each level 1 cell type.

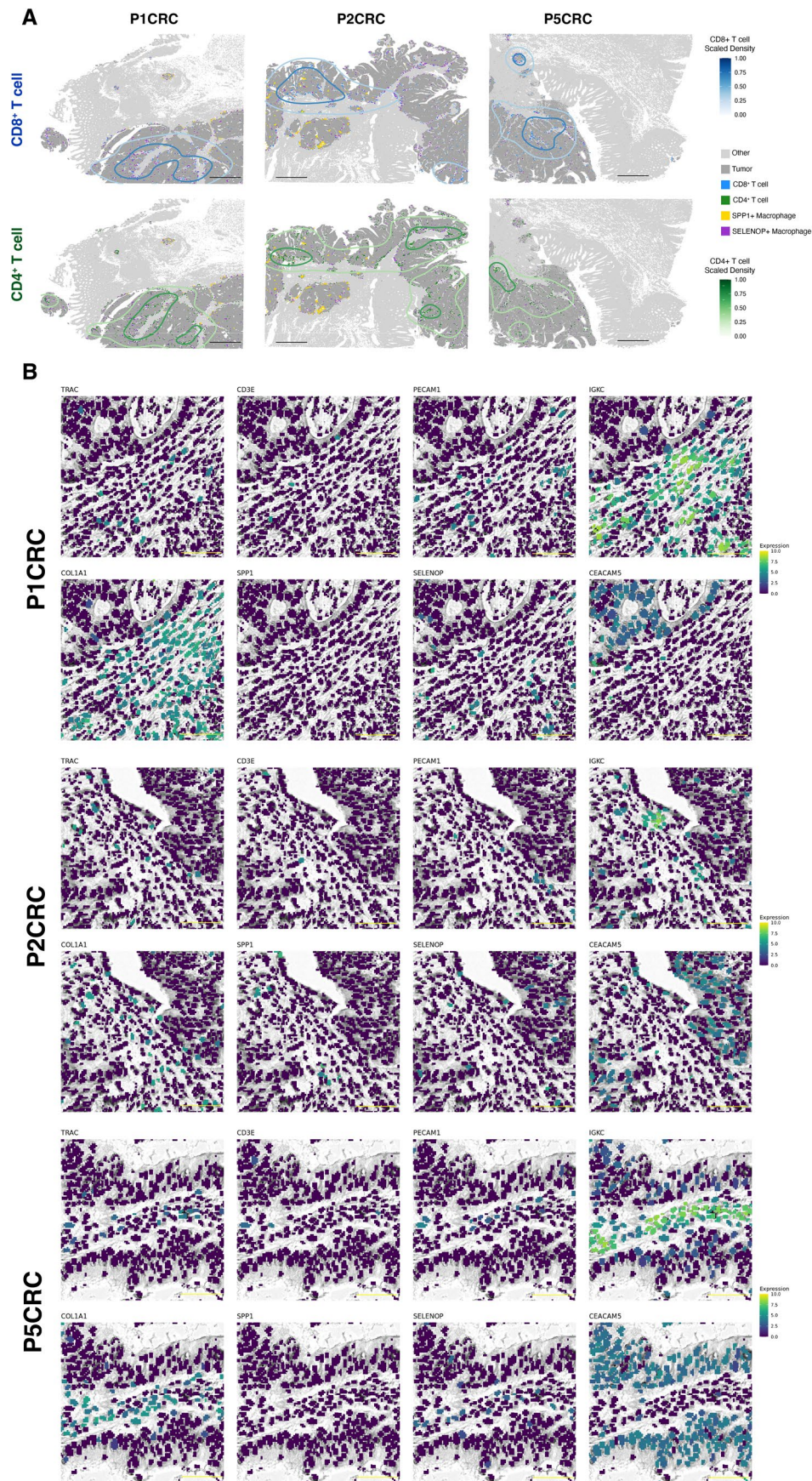


Extended Data Fig. 7 | Analysis of macrophage subpopulations in normal and tumor regions of colon cancer sections. a. Dot plot denoting the expression of differentially expressed genes in the 4 macrophages cluster identified via unsupervised clustering. **b.** Barplot with the proportion of each macrophage cluster. Colors represent distance to the tumor. **c.** Barplot with the proportion

of each macrophage cluster. Colors represent the different samples. **d.** Spatial organization of the 4 identified macrophage populations in the colon cancer samples. Shades of gray represent normal and tumor regions in the section and colors represent the identified unsupervised clusters. Scale bars = 1mm.

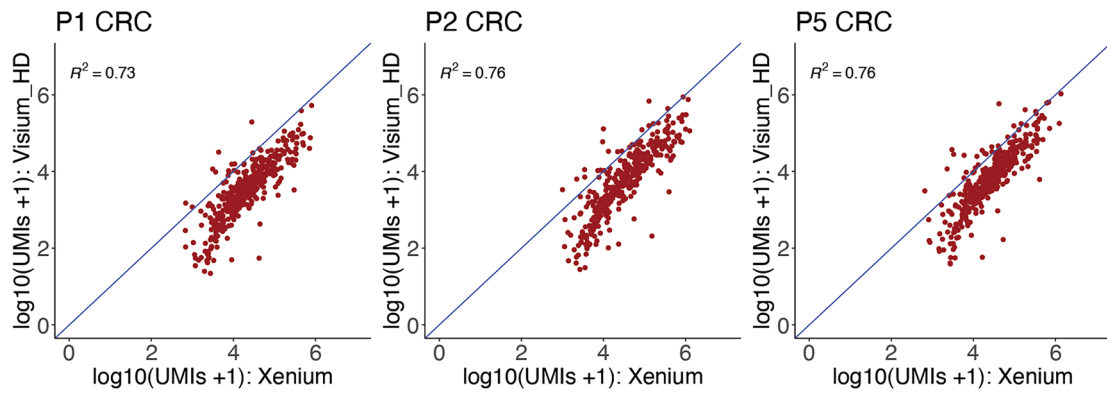


Extended Data Fig. 8 | Deconvolution class for 8 μ m bins labeled as T cells. Barplots denoting the deconvolved class for CD4 T cells and CD8 T cells in the 50 micron TME and rest of the tissue for each patient (n=3).



Extended Data Fig. 9 | Localization of CD4 and CD8 T cells. **a.** Kernel density maps showing the differential spatial localization of CD4 and CD8 T cells in the CRC sections (n = 3). **b.** Expression of TRAC (T cell), CD3E (T cell), PECAM1 (Endothelial), IGKC (Plasma), COL1A1 (CAF), SPP1 (Macrophage), SELENOP

(Macrophage) and CEACAM5 (Tumor) in the segmented nuclei for each patient. UMI counts were grouped by 2 micron bins located within each segmented nuclei. Scale bars: black = 1mm; yellow = 50µm.



Extended Data Fig. 10 | Cross-platform Sensitivity. Sensitivity comparisons between Visium HD and Xenium in situ gene expression data have been performed on serial sections from the same colon cancer FFPE blocks in a subset of 3 CRC samples. Plots show per gene pseudo bulk correlation between paired Visium HD (UMI counts) and Xenium in situ (gene counts) data. Xenium is on average 5.7x more sensitive on a per-gene basis than Visium HD for genes

included in both panels at the sequencing depth used (range: 1309-1865 reads per 8 μ m bin). Sensitivity was calculated by taking the geometric mean of the per gene fold difference between Visium HD and Xenium counts. Comparison of transcript diversity in the shared region found that Visium HD exhibited, on average, ~6.5x more transcripts than Xenium. See Supplementary Table 5.

Reporting Summary

Nature Portfolio wishes to improve the reproducibility of the work that we publish. This form provides structure for consistency and transparency in reporting. For further information on Nature Portfolio policies, see our [Editorial Policies](#) and the [Editorial Policy Checklist](#).

Statistics

For all statistical analyses, confirm that the following items are present in the figure legend, table legend, main text, or Methods section.

- | | |
|-------------------------------------|--|
| n/a | Confirmed |
| <input type="checkbox"/> | <input checked="" type="checkbox"/> The exact sample size (n) for each experimental group/condition, given as a discrete number and unit of measurement |
| <input type="checkbox"/> | <input checked="" type="checkbox"/> A statement on whether measurements were taken from distinct samples or whether the same sample was measured repeatedly |
| <input type="checkbox"/> | <input checked="" type="checkbox"/> The statistical test(s) used AND whether they are one- or two-sided
<i>Only common tests should be described solely by name; describe more complex techniques in the Methods section.</i> |
| <input type="checkbox"/> | <input checked="" type="checkbox"/> A description of all covariates tested |
| <input type="checkbox"/> | <input checked="" type="checkbox"/> A description of any assumptions or corrections, such as tests of normality and adjustment for multiple comparisons |
| <input type="checkbox"/> | <input checked="" type="checkbox"/> A full description of the statistical parameters including central tendency (e.g. means) or other basic estimates (e.g. regression coefficient) AND variation (e.g. standard deviation) or associated estimates of uncertainty (e.g. confidence intervals) |
| <input checked="" type="checkbox"/> | <input type="checkbox"/> For null hypothesis testing, the test statistic (e.g. F , t , r) with confidence intervals, effect sizes, degrees of freedom and P value noted
<i>Give P values as exact values whenever suitable.</i> |
| <input checked="" type="checkbox"/> | <input type="checkbox"/> For Bayesian analysis, information on the choice of priors and Markov chain Monte Carlo settings |
| <input checked="" type="checkbox"/> | <input type="checkbox"/> For hierarchical and complex designs, identification of the appropriate level for tests and full reporting of outcomes |
| <input checked="" type="checkbox"/> | <input type="checkbox"/> Estimates of effect sizes (e.g. Cohen's d , Pearson's r), indicating how they were calculated |

Our web collection on [statistics for biologists](#) contains articles on many of the points above.

Software and code

Policy information about [availability of computer code](#)

Data collection Data was collected using 10x Genomics analysis pipelines which are all publicly available, including: Space Ranger v3.0., Cell Ranger v8.0.0, Xenium Onboard Analysis pipeline v2.0.0, Loupe Browser v8.0

Data analysis Data was analysed using 10x Genomics analysis pipelines which are all publicly available, including: Space Ranger v3.0, Cell Ranger v8.0.0, Xenium Onboard Analysis pipeline v2.0.0. Software (R or Python packages): Seurat v5, spacr v2.2.1, stardist v0.9.0 and LIANA v0.1.12 were used for downstream analysis. Custom scripts used for this paper are available on GitHub at: https://github.com/10XGenomics/HumanColonCancer_VisiumHD All code has also been deposited at Zenodo <https://zenodo.org/records/15042463> All details are outlined in the Methods section and third party tools are referenced.

For manuscripts utilizing custom algorithms or software that are central to the research but not yet described in published literature, software must be made available to editors and reviewers. We strongly encourage code deposition in a community repository (e.g. GitHub). See the Nature Portfolio [guidelines for submitting code & software](#) for further information.

Data

Policy information about [availability of data](#)

All manuscripts must include a [data availability statement](#). This statement should provide the following information, where applicable:

- Accession codes, unique identifiers, or web links for publicly available datasets
- A description of any restrictions on data availability
- For clinical datasets or third party data, please ensure that the statement adheres to our [policy](#)

All datasets generated in this manuscript are available for download here: <https://www.10xgenomics.com/products/visium-hd-spatial-gene-expression/dataset-human-crc>

For enrichment analysis we used the MSigDB_Hallmark_2020: <https://www.gsea-msigdb.org/gsea/msigdb/human/genesets.jsp?collection=H>

We have uploaded the data to Gene Expression Omnibus (GEO) under accession number GSE280318

Data deposited at GEO contains raw data (fastq files) and processed data for the 8 micron bin size. Data available for download at the 10x Genomics website includes the all outputs from spaceranger, including the results for all bin sizes.

Research involving human participants, their data, or biological material

Policy information about studies with [human participants or human data](#). See also policy information about [sex, gender \(identity/presentation\), and sexual orientation](#) and [race, ethnicity and racism](#).

Reporting on sex and gender	Not considered in study design due to limited sample number.
Reporting on race, ethnicity, or other socially relevant groupings	Not considered in study design as this information was not available.
Population characteristics	Not considered in study design, information is included in Table 1 but was not considered in the analysis.
Recruitment	Samples were obtained via a commercial vendor (Discovery Life Sciences).
Ethics oversight	Human biological samples were obtained from Discovery Life Sciences. The research use of these specimens was approved by the corresponding Institutional Review Boards (IRB) under protocol numbers DLS-BB044-v.1 and SB-GP_v1. All patients provided written informed consent to Discovery Life Sciences for the research use of their biological samples.

Note that full information on the approval of the study protocol must also be provided in the manuscript.

Field-specific reporting

Please select the one below that is the best fit for your research. If you are not sure, read the appropriate sections before making your selection.

Life sciences Behavioural & social sciences Ecological, evolutionary & environmental sciences

For a reference copy of the document with all sections, see [nature.com/documents/nr-reporting-summary-flat.pdf](https://www.nature.com/documents/nr-reporting-summary-flat.pdf)

Life sciences study design

All studies must disclose on these points even when the disclosure is negative.

Sample size	No statistical methods were used to predetermine sample size. We selected samples that were all classified as colorectal adenocarcinoma, pre-treatment, on the basis of availability. We included samples from 5 patients, for 3 of these patients we were able to obtain samples from tumor, normal adjacent tissue (NAT), and dissociated tumor cells (DTC).
Data exclusions	None
Replication	Visium HD experiments were performed on one replicate per patient sample included (as described in Methods and Figure legends). Findings were validated using an orthogonal spatial platform (Xenium in situ) for selected samples (as described in Methods and Figure legends).
Randomization	Not relevant due to limited sample number.
Blinding	Not relevant due to limited sample number.

Reporting for specific materials, systems and methods

We require information from authors about some types of materials, experimental systems and methods used in many studies. Here, indicate whether each material, system or method listed is relevant to your study. If you are not sure if a list item applies to your research, read the appropriate section before selecting a response.

Materials & experimental systems

n/a	Involvement in the study
<input checked="" type="checkbox"/>	<input type="checkbox"/> Antibodies
<input checked="" type="checkbox"/>	<input type="checkbox"/> Eukaryotic cell lines
<input checked="" type="checkbox"/>	<input type="checkbox"/> Palaeontology and archaeology
<input checked="" type="checkbox"/>	<input type="checkbox"/> Animals and other organisms
<input checked="" type="checkbox"/>	<input type="checkbox"/> Clinical data
<input checked="" type="checkbox"/>	<input type="checkbox"/> Dual use research of concern
<input checked="" type="checkbox"/>	<input type="checkbox"/> Plants

Methods

n/a	Involvement in the study
<input checked="" type="checkbox"/>	<input type="checkbox"/> ChIP-seq
<input checked="" type="checkbox"/>	<input type="checkbox"/> Flow cytometry
<input checked="" type="checkbox"/>	<input type="checkbox"/> MRI-based neuroimaging

Plants

Seed stocks	<i>Report on the source of all seed stocks or other plant material used. If applicable, state the seed stock centre and catalogue number. If plant specimens were collected from the field, describe the collection location, date and sampling procedures.</i>
Novel plant genotypes	<i>Describe the methods by which all novel plant genotypes were produced. This includes those generated by transgenic approaches, gene editing, chemical/radiation-based mutagenesis and hybridization. For transgenic lines, describe the transformation method, the number of independent lines analyzed and the generation upon which experiments were performed. For gene-edited lines, describe the editor used, the endogenous sequence targeted for editing, the targeting guide RNA sequence (if applicable) and how the editor was applied.</i>
Authentication	<i>Describe any authentication procedures for each seed stock used or novel genotype generated. Describe any experiments used to assess the effect of a mutation and, where applicable, how potential secondary effects (e.g. second site T-DNA insertions, mosaicism, off-target gene editing) were examined.</i>